nature reviews methods primers

https://doi.org/10.1038/s43586-025-00391-1

Primer

Check for updates

Interferometric scattering microscopy

Naomi S. Ginsberg[1,2,3,4], Chia-Lung Hsieh[5], Philipp Kukura[6,7], Marek Piliarik[8] & Vahid Sandoghdar[9,10,11]

Abstract

Over the past two decades, interferometric scattering (iSCAT) microscopy has become a powerful label-free imaging method with a range of applications in fundamental science and technology. iSCAT detects the scattering of subwavelength entities through interference with a reference beam of light. Performed in a variety of illumination and detection schemes, iSCAT has exploited both amplitude and phase information to reach single-molecule detection sensitivity; to determine the size, mass and refractive index of nanoparticles; to achieve high spatiotemporal precision in 3D tracking of nanoparticles; to image subcellular nanostructures; and to quantify ultrafast diffusion and transport of energy in solids. In this Primer, we describe the basic principles of iSCAT detection and imaging from theoretical and practical points of view. We discuss various factors that affect the attainable signal-to-noise ratio, which in turn determines crucial performance features such as sensitivity and speed. We survey selected applications in which iSCAT has been instrumental in providing new insights. Finally, we discuss some of the current challenges and potential avenues for advancing the technique further.

Sections

[1]Departments of Chemistry and Physics, University of California Berkeley, Berkeley, CA, USA. [2]Materials Science Division, Chemical Science Division and Molecular Biophysics and Integrated Bioimaging Division, Lawrence Berkeley National Laboratory, Berkeley, CA, USA. [3]STROBE, National Science Foundation Science and Technology Center, University of California Berkeley, Berkeley, CA, USA. [4]Kavli Energy NanoSciences Institute at Berkeley, Berkeley, CA, USA. [5]Institute of Atomic and Molecular Sciences, Academia Sinica, Taipei, Taiwan. [6]The Kavli Institute for Nanoscience Discovery, University of Oxford, Oxford, UK. [7]Physical and Theoretical Chemistry Laboratory, Department of Chemistry, University of Oxford, Oxford, UK. [8]Institute of Photonics and Electronics of the Czech Academy of Sciences, Prague, Czech Republic. [9]Max Planck Institute for the Science of Light, Erlangen, Germany. [10]Max-Planck-Zentrum für Physik und Medizin, Erlangen, Germany. [11]Department of Physics, Friedrich-Alexander University Erlangen–Nürnberg, Erlangen, Germany. e-mail: vahid.sandoghdar@mpl.mpg.de

Introduction

The principal task of optical microscopy is to detect, image and resolve the microscopic and nanoscopic structure and dynamics of a specimen. Through the advent of near-field microscopy and super-resolution fluorescence microscopy, the issue of resolution has attracted a great deal of attention in the past three decades[1]. Sensitivity in fluorescence microscopy was also improved to the level of single molecules in the same period[2]. However, various restrictions associated with fluorescence imaging, such as photobleaching, the need for labelling, and phototoxicity, have prompted efforts to push the limits of fluorescence-free microscopy. One common approach in this respect uses nonlinear optical effects[3], although these struggle to reach single-molecule sensitivity.

A particularly sensitive approach uses optical interference, which efficiently translates even the smallest variations in the phase of an electromagnetic field into a detectable intensity change[4]. The use of interferometry in imaging dates back to the nineteenth century[5], but the exploitation of the phase of light in microscopy became established in the later part of the twentieth century with the advent of phase contrast microscopy[6,7], differential interference microscopy[8], interference reflection microscopy[9], quantitative phase imaging[10], digital holography[11] and their many variants. The key underlying mechanism of these methods – interference – is also fundamental to conventional bright-field microscopy, which has been used to visualize cell features at close to diffraction-limited resolution for over 350 years[12,13].

To establish the generality of interference as an imaging mechanism, let us consider an interface between two half spaces and assume normal-incidence illumination $\mathbf{E}_{inc}$ for the sake of simplicity (Fig. 1a). In reflection, we detect this interface through the intensity of light which it reflects, $I_{refl} \propto |\mathbf{E}_{refl}|^2$. Here, $\mathbf{E}_{refl} = r\mathbf{E}_{inc}$ denotes the reflected field with r denoting the field reflectivity obtained from Fresnel coefficients[4]. If we now attribute an electric field $\mathbf{E}_{obj}$ to the response of the object, we can write $\mathbf{E}_{refl} = \mathbf{E}_{obj}$ on a detector placed in the reflection path. Matching the tangential electric field at the two sides of the interface yields the transmitted field, $\mathbf{E}_{inc} + \mathbf{E}_{obj} = \mathbf{E}_{trans}$. Thus, in the forward direction we obtain the detected intensity

$$I_{det} \propto |\mathbf{E}_{inc} + \mathbf{E}_{obj}|^2 = |\mathbf{E}_{inc}|^2 + |\mathbf{E}_{obj}|^2 + 2|\mathbf{E}_{inc}||\mathbf{E}_{obj}|\cos\varphi, \quad (1)$$

where φ denotes the phase difference between $\mathbf{E}_{inc}$ and $\mathbf{E}_{obj}$. From this perspective, the detected transmission signal in bright-field imaging results from the coherent sum of the electric fields $\mathbf{E}_{inc}$ and $\mathbf{E}_{obj}$. The phase of the field $\mathbf{E}_{obj}$ radiated by the object generally depends on the wavelength of illumination, as the refractive index of material is generally a function of wavelength.

If we now consider a slab of refractive index n and thickness L, the same general treatment can be applied, although the effect of multiple reflections at its two interfaces would need to be considered (Fig. 1b). If we then shrink the slab to subwavelength dimensions in all directions (Fig. 1c–f), the strength of the interaction between the object and light, represented by the field $\mathbf{E}_{obj}$, decreases. Below a certain object size, the signal becomes too small to be detected, particularly in the presence of non-negligible background light.

The interaction of an object with an incident electromagnetic field results in internal and external fields that can be computed by solving Maxwell's equations and accounting for the appropriate boundary conditions. For a spherical object, the solution entails a series of multipoles[14]. As the size of the particle and its refractive index mismatch with respect to its surrounding medium become smaller, fewer modes contribute until only the dipolar mode remains. When approaching particle diameters of the order of 10% of the incident wavelength or less – known as the Rayleigh scattering regime – the response of the particle can be formulated in terms of its polarizability, α (Box 1). For a simplified spherical particle, α is given in cgs units by

$$\alpha = 3V\left(\frac{\varepsilon_p - \varepsilon_m}{\varepsilon_p + 2\varepsilon_m}\right), \quad (2)$$

where V denotes the particle volume, and ε_p and ε_m are the complex dielectric functions of the particle and its surrounding medium, respectively (Box 2).

The electric field scattered by a nano-object ($\mathbf{E}_{sca}$) is proportional to the incident electric field, $\mathbf{E}_{sca} \propto \alpha\mathbf{E}_{inc}$. Importantly, V dictates the strength of $\mathbf{E}_{sca}$: a small change in the lateral dimensions of the nano-object translates to a large modification of α. The variations of ε_p and ε_m for different materials, on the other hand, usually lead to a modest change in α. This relationship has been and continues to be used extensively to determine the mass and size of nanoparticles at the ensemble level, for example by multiple-angle light scattering[15]. The quadratic scaling of the scattered light intensity with the volume (proportional to the square modulus of equation (2)), however, requires prior chromatographic separation for the characterization of mixtures. Although early implementations of interference microscopy managed to detect submicrometre-sized objects[16–18], explicit studies of individual nanoparticles and their exploitation in applications remained elusive for a long time.

It was the emergence of a new era of nanoscience in the 1990s that reinforced the need for the detection of single molecules and nanoparticles. In particular, single gold nanoparticles (GNPs) were the focus of much investigation in the context of scanning near-field optical microscopy[19,20] and photothermal spectroscopy[21]. Later, single GNPs as small as 5 nm were shown to be detected in reflection[22] and transmission[23]. By describing the detection process as an interference phenomenon following equation (1), Lindfors and colleagues introduced interferometric scattering (iSCAT) microscopy, explaining the role of particle polarizability and addressing fundamental noise issues[22]. The key advance was not critical changes to the experimental approach but rather that individual nanoparticles could be imaged, detected and studied by light scattering alone. This phenomenon has defined iSCAT and differentiates it from prior interference microscopy implementations. Metallic nanoparticles are now routinely used to track the dynamics of labelled molecules, both in vitro and on cells[24–29], and single quantum dots[30,31], dye molecules[32,33] and proteins[34,35] can be directly detected, leading to the development of mass photometry[36]. The improved detection sensitivity ushered in by iSCAT is also influencing applications in light microscopy, including ultrafast dynamics in semiconductors and 2D materials[37–39], chemical reactions[40] and the inner working of cells[41,42].

Single colloidal semiconductor quantum dots[31] and even (quenched) dye molecules[32,33] have been detected directly with reflection and transmission, respectively. These studies exploited the absorption resonance of the quantum emitter to enhance the extinction cross section beyond what would be expected from its size. By eliminating phonon dephasing processes, cryogenic measurements resulted in further substantial enhancement of the resonant cross section, leading to extinction signals as large as approximately 10% in transmission[30,43,44]. These measurements established an important link between Rayleigh

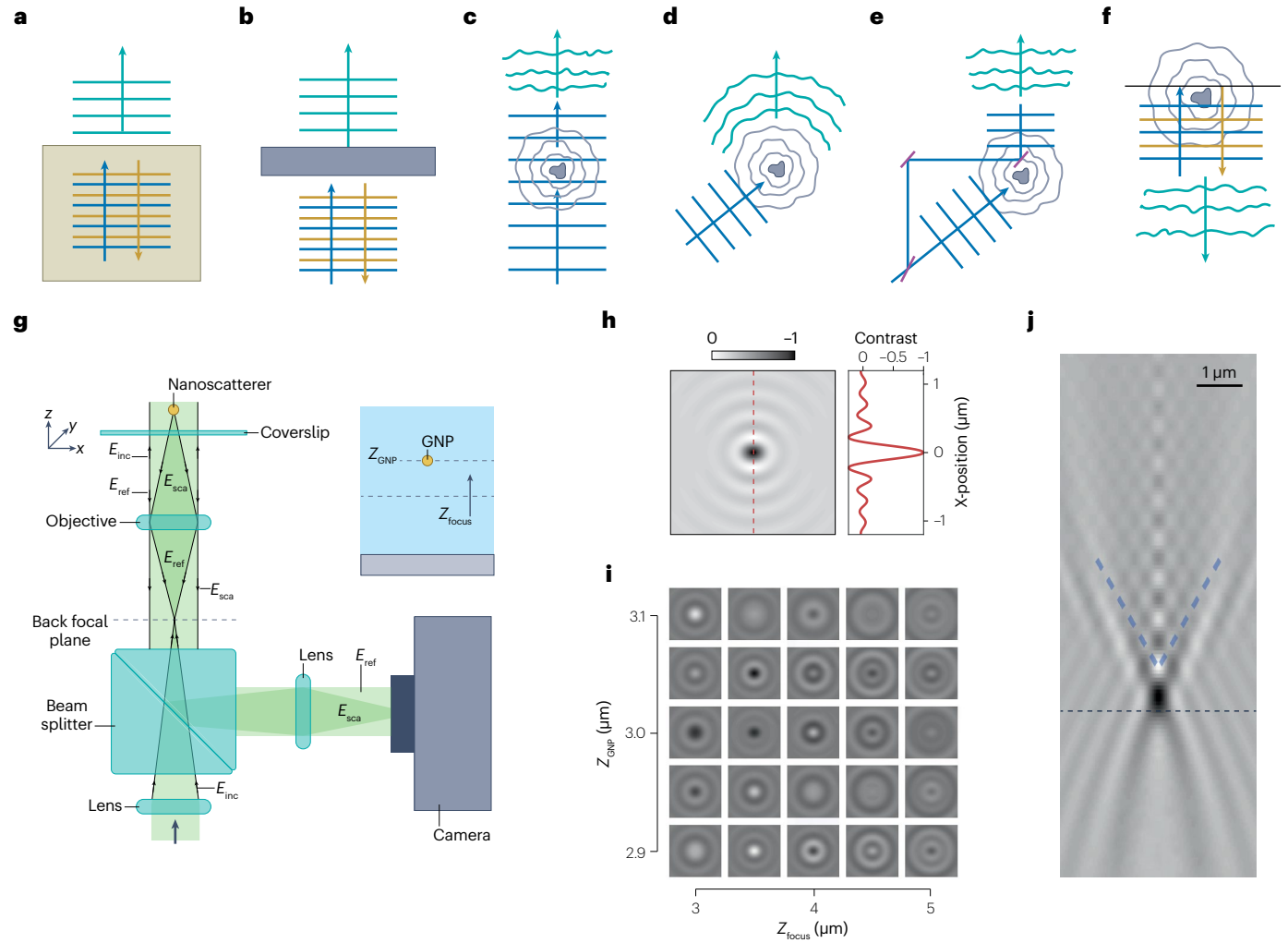

Fig. 1 | iSCAT microscopy. a–**f**, Various schemes for illumination and detection in scattering microscopy: interface between two half-spaces of different materials (panel **a**); a macroscopic slab (panel **b**); and a nano-object (panels **c**–**f**). Schemes show macroscopic transmission measurements (panels **a** and **b**), transmission interferometric scattering (iSCAT) (panel **c**), dark-field microscopy (panel **d**), holography (panel **e**) and reflection iSCAT (panel **f**). The colour scheme indicates blue for illumination, orange for reflection, grey for scattered light and teal for detected light. **g**, An illustration of a typical wide-field reflection iSCAT set-up. The inset depicts a nanoparticle at a certain height above the substrate. **h**, A lateral interferometric point spread function (iPSF) of a single subwavelength scatterer in wide-field mode. The cross section along the dashed line is shown on the right-hand side. **i**, An array of different iPSFs as the nanoparticle and the objective focus are displaced in the axial direction. **j**, An iPSF along the x–z plane, if the focus is scanned along z (see panel **g**). The blue dashed lines act as a guide to the eye for one of the sidelobes. GNP, gold nanoparticle. Panels **g**, **i** and **j** adapted with permission from ref. 88, © Optica Publishing Group. Panel **h** reprinted from ref. 69, CC BY 4.0.

scattering, which is commonly known from subwavelength particles, and the radiation of individual quantum emitters[45]. Furthermore, as the refractive index of a bulk material is also based on the response of its individual atomic constituents[4], scattering from nanoscopic components can be seen as the fundamental process that leads to reflection, as exemplified by macroscopic electromagnetic theory (Box 3).

In this Primer, we discuss the key components of iSCAT microscopy instrumentation, beginning with the underlying physics of the iSCAT signal and the sources of its fluctuations. Although technical details such as the choice of the optomechanical components are not extensively covered, we highlight sources of noise and other issues that must be considered in experimental design. We further discuss applications in which the iSCAT signal has been used to obtain various types of information about nanoparticles, such as their size, mass, refractive index and 3D location. A particular emphasis is placed on exploring and pushing the measurement limits of iSCAT. We then present several application areas in which these capabilities have been used across a range of scientific disciplines. We conclude by commenting on the reproducibility of the data, limitations of the method and several exciting potential avenues for future developments.

Experimentation

Here, we discuss the central concepts and features that should be considered in an iSCAT experiment. Starting with the definition of

the signal that is measured, we consider various aspects of the instrumentation with emphasis on the illumination and detection criteria. Furthermore, we review factors that might modulate the signal as well as issues concerning signal-to-noise ratio (SNR).

iSCAT signal

The signals in fluorescence and dark-field microscopy represent the intensity of light stemming from an object and are therefore positive. In iSCAT, however, the response of the object is expressed by $|\mathbf{E}_{obj}|^2 + 2|\mathbf{E}_{inc}||\mathbf{E}_{obj}|\cos\varphi$ (equation (1)), which modulates the baseline $|\mathbf{E}_{inc}|^2$ and can take on positive or negative values. Given that this signal is proportional to the intensity of the incident beam, one expresses it in terms of a relative contrast C given by

$$C = \frac{I_{det} - I_{ref}}{I_{ref}} = \frac{|\mathbf{E}_{sca}|^2 + 2|\mathbf{E}_{sca}||\mathbf{E}_{ref}|\cos\varphi}{|\mathbf{E}_{ref}|^2} \approx 2\frac{|\mathbf{E}_{sca}|}{|\mathbf{E}_{ref}|}\cos\varphi, \quad (3)$$

where I_{ref} and $\mathbf{E}_{ref}$ denote the intensity and field of a reference beam that is interfered with the scattered light, respectively. Here, we assume that $|\mathbf{E}_{sca}|^2 \ll 2|\mathbf{E}_{sca}||\mathbf{E}_{ref}|$, which holds for particles with small enough α and the absence of any background scattering. In this case, the term $|\mathbf{E}_{sca}|^2$ (corresponding to dark-field microscopy; Fig. 1d), which scales as V^2, is negligible compared with the interference term that scales as V. It should, however, be kept in mind that the condition for $|\mathbf{E}_{sca}| \ll |\mathbf{E}_{ref}|$ to hold also depends on the choice of $\mathbf{E}_{ref}$ which we relate to $\mathbf{E}_{inc}$ via $\mathbf{E}_{ref} = r\mathbf{E}_{inc}$. In the case of a reflection-mode instrument, r simply represents the substrate field reflectivity[22]. If we now express the scattered field as $\mathbf{E}_{sca} = s\mathbf{E}_{inc}$, we obtain

$$C = 2\frac{s}{r}\cos\varphi, \quad (4)$$

where s denotes an effective multiplicative factor that accounts for many factors such as the polarizability, collection efficiency and so on. Similarly, we assume that r also includes the contributions of all other processes that reduce the strength of the reference field with respect to the incident field.

Instrument layout

Single-molecule fluorescence experiments can be performed in different illumination arrangements, such as wide-field mode or beam scanning mode, and with various detection schemes using cameras or point detectors. Similarly, interferometric measurements can be performed in different configurations. In the most used schemes of iSCAT studies, the reference beam is carried in transmission (Fig. 1c), introduced externally (Fig. 1e) or generated as a reflected component of the incident beam (Fig. 1f). In a transmission arrangement, the incident wave and parts of the scattered component are collected using a microscope objective, and their interferogram is projected through a tube lens onto the detector placed in the image plane. In the reflection arrangement, the incident beam partially reflects from the substrate and is collected by the microscope objective along with the back-scattered portion of the light from the nano-object. This light is reflected from a beam splitter and is imaged onto the detector. The combination of the microscope objective and tube lens determines the overall magnification factor of the interferogram in the image plane. External reference beams are often mixed with the transmission signal, such as in the case of conventional holographic arrangements[16,46], but they can also be introduced in other ways[47].

It follows from equation (4) that a change in the phase shift φ of one-quarter of the wavelength is sufficient to lower the iSCAT signal from its maximum to zero, making the contrast sensitive to even a small path change of 1 nm. Thus, to reduce the susceptibility of the signal to mechanical and to environmental changes, φ should be kept constant. In transmission, there is no path difference between $\mathbf{E}_{sca}$ and $\mathbf{E}_{ref}$, which is simply the transmitted part of $\mathbf{E}_{inc}$. This strategy offers φ a high degree of intrinsic stability, although in practice, fluctuations of the Gouy phase might compromise stability (Box 1). Interferometers that use an external reference beam, however, require active stabilization or a means for referencing between individual channels[47]. Reflection iSCAT offers the advantage that for nano-objects very close to the microscope substrate, $\mathbf{E}_{ref}$ and $\mathbf{E}_{sca}$ also experience a common path, leading to a highly stable φ (ref. 22).

In Fig. 1g, we depict the arrangement of the most crucial components for the case of linearly polarized illumination in wide-field and detection in reflection mode. The simplicity of an iSCAT microscope greatly contributes to the versatility and wide application range of

Box 1 | Extinction and the optical theorem

Let us consider an incident field $\mathbf{E}_{inc}$ along the x direction, normal to its propagation axis z. The superposition principle states that after interaction with a point dipole oriented along x, the field $\mathbf{E}_{det}$ at the detection screen placed at a large distance behind the dipole is given by the sum $\mathbf{E}_{det} = \mathbf{E}_{inc} + \mathbf{E}_{dip}$, where $\mathbf{E}_{dip}$ is the electric field radiated by the dipole also oriented along the x axis.

In an intuitive picture based on energy conservation, the energy associated with the light waves with wavevector along the propagation axis of $\mathbf{E}_{inc}$ is monitored. The energy that is missing in transmission is either absorbed or scattered. Because conventional detectors can only measure the intensity of light, we formulate the total detected intensity I_{det} as

$$I_{det} \propto |\mathbf{E}_{inc} + \mathbf{E}_{dip}|^2 = I_{inc} + I_{dip} + 2|\mathbf{E}_{inc}||\mathbf{E}_{dip}|\cos\varphi. \quad (5)$$

The first term given by I_{inc} is simply the intensity of the incident light. The second term I_{dip} reports on the intensity of the light that is radiated by the dipole. The third term results from the interference of the two electric fields, whereby the phase $\varphi = \varphi_{inc} - \varphi_{dip}$ describes the phase difference between $\mathbf{E}_{inc}$ and $\mathbf{E}_{dip}$.

The relative phase φ derives from the different geometry of the incident light wave and the dipolar radiation. In the common textbook treatment using an incident plane wave, the phase of the dipolar wave is shifted by π/2 with respect to that of the plane wave φ_{inc} (ref. 70). When dealing with confined beams, the Gouy phase φ_G must also be considered, which applies when wavevector components of the beam experience different path lengths[4]. In the case of a Gaussian wave, φ_G corresponds to π/2 between the tightest waist of the wave and infinity.

In addition, as is familiar in the context of a driven oscillator, the phase φ_{dip} of a resonant dipole experiences a lag of π/2 with respect to its driving fields. In real-world materials, φ_{dip} is determined by the imaginary part of the polarizability[70]. The collective effect of all of the different contributing phases results in a total phase φ, which determines the interference contrast. In the ideal case of a dipolar incident wave, the total phase shift between φ_{dip} and φ_{inc} amounts to π, resulting in completely destructive interference[171].

the method. Technical details such as strategies for simple alignment, choices of the optical and mechanical components, and care for mechanical stability can be found elsewhere[48,49]. Here, we focus on the conceptual foundation of the iSCAT instrument.

Illumination

Similar to fluorescence microscopy, iSCAT illumination can be realized in several ways. These include arrangements in which a laser beam is tightly focused by a high-numerical-aperture microscope objective[22,33,41], wide-field illumination by focusing the light at the back focal plane of the objective[34], wide-field illumination by rapid scanning of a focused beam[50], illumination via total internal reflection[47] or the incident field being launched into surface plasmons[51,52]. The optimal choice of light source depends on several factors, and various sources can be used for illumination as long as a sufficient degree of coherence between $\mathbf{E}_{ref}$ and $\mathbf{E}_{sca}$ is guaranteed at the location of the detector. Here, longitudinal coherence and transverse coherence must be distinguished from each other.

Longitudinal coherence. Interference takes place when two fields have a well-defined phase with respect to each other (Box 4). For this to be possible, the path difference between the two arms of an interferometer cannot be longer than the 'longitudinal coherence length' of the light source used[4]. When imaging nano-objects on a glass substrate in a common-path reflection iSCAT mode, nearly any light source would be sufficiently coherent because the effective path length difference between $\mathbf{E}_{ref}$ and $\mathbf{E}_{sca}$ is in the nanometre range. Other applications and arrangements of the reference beam use a light source with a sufficiently long coherence length. Typical single-mode lasers have linewidths of 10 GHz or less, leading to coherence lengths larger than 7 mm. In comparison, a light-emitting diode (LED) with a spectral width of 20 nm has a coherence length of 7 µm, which can be sufficient in some applications and can be convenient to eliminate background interference fringes from larger containers in which a sample is prepared.

Transverse coherence. In addition to the longitudinal coherence length, the transverse degree of coherence should also be considered. Although all points on a wavefront of a single-mode laser beam have the same phase, this might not be true for other sources. For example, the phase of a spot generated by an extended light source such as an LED or a lamp filament is not uniform because photons emitted at different lateral locations are not correlated[4]. This is the reason that one usually uses a small pinhole to establish a good spatial coherence before observing interference fringes in a Young's double-slit experiment. A source with partial transverse coherence leads to the reduction of the fringe contrast[4]. The transverse coherence can be manipulated through fast scanning of a laser focus across the field of view, such as by using an acousto-optic deflector[50]. In this case, the transverse coherence is determined by the size of the focused beam. Alternatively, a rotating diffuser has been used to tailor the degree of transverse coherence[53].

Wavelength. Another important feature of the light source is its wavelength, λ. If the nano-object supports resonances, as is the case for gold or silver nanoparticles, dye molecules or semiconductor quantum dots, it is favourable to tune λ to an electronic resonance to enhance the polarizability. For dielectric particles in the Rayleigh scattering regime, such as single proteins, it is advantageous to choose the shortest possible λ, given the $1/\lambda^4$ scaling of the scattering cross section (Box 2). Other effects such as photodamage, resonances of background species, response of detectors and availability of suitable optics must also be kept in mind.

In practice, a variety of light sources have been used to achieve a range of iSCAT measurements, including high-performance solid-state single-mode lasers[29], single-mode diode lasers[34], multimode diode lasers[36] and white-light single-mode sources based on supercontinuum generation[22,28], as well as LEDs[54,55]. Ultrafast time-resolved studies have been carried out using pulsed lasers with picosecond and femtosecond pulse durations[37–39,56–68].

Intensity. The intensity of the incident light is not an important a priori parameter in iSCAT measurements because the signal is expressed in terms of a contrast (equation (4)). However, intensity has a decisive role in practice because the number of detected photons determines the achievable SNR and imaging speed[69]. Furthermore, potential

Box 2 | Polarizability and cross sections for absorption and scattering

When an electric field $\mathbf{E}_{inc}$ impinges on an object that is much smaller than the wavelength of light, such as a nano-object, it polarizes the material and induces a dipole moment[70]. The resulting dipole oscillates at the frequency of the incident light and reradiates at the same frequency. The strength of $\mathbf{E}_{obj}$ is determined by the polarizability (α) of the nano-object[70]. This quantity depends on the shape and material of the particle as well as its surrounding.

The complex quantity α is directly related to the scattering and absorption cross sections of the nano-object at wavelength λ_m in the medium:

$$\sigma_{sca} = \frac{8\pi^2 |\alpha|^2}{3\lambda_m^4} \quad (6)$$

$$\sigma_{abs} = \frac{2\pi \mathrm{Im}(\alpha)}{\lambda_m}. \quad (7)$$

The scattered field $\mathbf{E}_{sca}$ not only reports on the scattering cross section but also on the absorption of the nanoparticle[70]. The polarizability is a complex quantity that affects both the amplitude and phase of $\mathbf{E}_{sca}$.

The polarizability of a non-spherical particle also includes information about its shape. Although in general it is not possible to express α in a closed form, the polarizability of an ellipsoidal nanoparticle can be derived analytically and is given by

$$\alpha_i = V\left[\frac{\varepsilon_p - \varepsilon_m}{\varepsilon_m + L_i(\varepsilon_p - \varepsilon_m)}\right], \quad (8)$$

where L_i signifies a depolarization factor along the ith coordinate axis, and ε_p and ε_m represent the dielectric functions of the particle and its surrounding medium, respectively. For a spherical particle, $L_i = 1/3$. It thus follows that an ellipsoidal particle with a given orientation scatters light beams of different polarizations to various degrees[71].

Box 3 | From scattering to reflection

Interferometric scattering (iSCAT) has sufficiently high sensitivity for detecting nanostructures, enabling imaging of single proteins[34,35,103], individual semiconductor quantum dots[31] and dye molecules[32,33] at room temperature without the need for fluorescence. Several single nano-objects spaced at distances less than a diffraction limit cannot be resolved individually. However, an effective polarizability α can be assigned to this small ensemble of scatterers so that the iSCAT signal provides insight into their density. If the extent of the active region increases beyond the relevant wavelength, the concept of polarizability transitions to that of susceptibility and refractive index[4]. This regime marks the transition from scattering from confined nanoscopic systems to reflection from macroscopic objects. In this light, iSCAT is to be understood as a size-sensitive version of interference reflection microscopy[41] capable of detecting objects significantly smaller than the illumination wavelength. This is analogous to the role of single-molecule fluorescence microscopy as the most sensitive version of conventional fluorescence microscopy.

photodamage incurred by the sample depends on the light intensity, as do residual detector nonlinearities.

Polarization. In the case of a spherical object, the polarizability α is insensitive to the polarization of the incident light[70]. If the dielectric function of the object has an anisotropic distribution, such as for ellipsoidal particles (Box 2), its light scattering is generally polarization dependent[29,70,71]. In such applications, the choice of polarization in the illumination and the detection paths can be used to optimize the signal.

Detection

The detection channel contains two important components, namely $\mathbf{E}_{sca}$ and $\mathbf{E}_{ref}$. Considering the weak scattering of individual nanoparticles, iSCAT detection is typically realized through a high-numerical-aperture microscope objective. In special cases, $\mathbf{E}_{sca}$ can be evanescently channelled through surface plasmon prisms or waveguides. The reference field can also be established in several ways[72,73]. In reflection iSCAT, $\mathbf{E}_{ref}$ is usually obtained from the interface between the sample and the cover glass. In transmission iSCAT, $\mathbf{E}_{ref}$ becomes equivalent to the incident field[26,33]. In a more generalized holographic arrangement (Fig. 1e), $\mathbf{E}_{ref}$ is produced by an external coherent beam[47]. These can be varied further in special cases; for example, light scattered from the interface of a nanochannel has been interfered with the scattering of a nano-object flowing in the nanochannel[74].

The choice of the detector is an important aspect of any microscopy experiment. Point detectors such as silicon photodiodes have been used in a confocal iSCAT layout. There is a large variety of these detectors, reaching all the way to single-photon sensitivity, and they can be operated down to the picosecond time window. Complementary metal–oxide–semiconductor (CMOS) cameras are usually used in a wide-field illumination scheme. These detectors have several technical limitations, particularly that there is an upper limit to the illumination intensity because camera pixels saturate beyond a certain point. Here, the pixel well depth, which is often expressed in units of electrons and ranges from 10^4 to 10^6, is an important consideration[69]. Cameras with larger well depths are favourable for iSCAT measurements.

Signal fluctuations due to noise. Ultrasensitive detection of weak scattering is a central mission of iSCAT. The detection sensitivity is limited by the ratio between the achievable contrast for a particular particle and the fluctuations in the image background over which the particle is to be detected. Unwanted fluctuations are usually referred to as noise, which can have many different origins. Noise is a statistical quantity and is therefore unpredictable. The most common noise encountered in microscopy originates from the detector or the light source.

In the case of the detector, the output can be accompanied by fluctuations that are not correlated with the signal that it measures. For example, dark noise denotes the noise that the detector registers in the absence of any light, which might arise from its active area or the electronics that amplify and process the signal. This noise usually adds to the signal level and does not scale with the signal strength[69]. In iSCAT, the incident light level is usually high enough that dark noise does not have an important role[5].

The detected signal can experience fluctuations due to the digitization process. For example, the signal from a 12-bit camera cannot be analysed with better precision than $\frac{1}{4{,}096} \simeq 2 \times 10^{-4}$. This precision can be improved by frame averaging. For an ideal linear-response shot noise-limited detector, the process of accumulation has the same effect on noise as increasing the full well capacity and the bit depth. Specifically, summing two consecutive frames results in an increase by a factor of $\sqrt{2}$ in the SNR limited by shot noise, effectively increasing the bit depth by 1.

Box 4 | Coherence

A central property of a wave is oscillation as a function of time and space with a well-defined phase φ. In the most elementary form, this is expressed as $\mathbf{E}(x, t) = \mathbf{E}_0 \cos\varphi(x, t)$, where $\varphi(t) = kx - \omega t$ describes a linear change of phase with time and space. In practice, the phase of a wave is not uniform over either space or time, leading to a finite degree of coherence.

Longitudinal coherence

Realistic light sources do not oscillate indefinitely; the oscillation phase is disrupted in a stochastic fashion. Coherence time τ is associated with the duration of continuous oscillations. Two wavefronts emitted at time differences much larger than τ are not correlated and do not interfere with each other. Following this terminology, a longitudinal coherence length can be defined by $c\tau$, where c denotes the speed of light. Alternatively, the coherence length can be expressed as $\lambda^2/2\Delta\lambda$, for wavelength λ and light source linewidth $\Delta\lambda$.

Transverse coherence

Aside from its longitudinal coherence, a light field is also characterized by the degree to which the phases of the electric fields are correlated over a given wavefront. Light emerging from a point leads to a high degree of transverse coherence because all points on the wavefront of a spherical wave have the same distance from the source, resulting in a common phase $\varphi(t) = kx - \omega t$. The electric field generated by a light-emitting diode (LED), however, is the sum of the fields originating from a wide range of points within the LED diameter of, say 100 µm, averaging out coherence effects.

A second important type of noise stems from the illumination source. Lasers, lamps and LEDs each have instrumental noise, which may originate from the underlying optical process or accompanying electronics. High-quality lasers can have root mean squared intensity fluctuations as low as 10^{-3} of their average value, but it is rare for a commercial laser to have intensity fluctuations lower than 10^{-4}, marking the contrast regime that becomes challenging for iSCAT studies. Intensity fluctuations can be monitored by diverting a small fraction of the incident beam onto a detector and accounting for the intensity noise of the light source. This information is then used as a reference to account for the intrinsic instrumental noise[22,32]. In wide-field imaging on a camera, the sum of the intensities over all pixels provides a convenient reference to monitor intensity fluctuations between frames[69].

In addition to instrumental or technical noise, measurements that count the number of quanta (photons in the case of iSCAT) typically encounter shot noise. In the limit of large numbers, the number N of randomly arriving quanta undergoes inherent fluctuations that follow a Gaussian distribution[4,5]. The characteristic full width at half-maximum σ of this distribution has a fixed relation to the mean number $\overline{N}$ of the profile given by $\sigma = \sqrt{\overline{N}}$. The implication of this fundamental phenomenon is that even if all external sources of signal fluctuations were to be eliminated, a given measurement is still subject to intrinsic statistical fluctuations in the number of detected photons. In other words, the higher the number of photons, the broader the distribution in their number. The ratio $\frac{N}{\sigma}$ of the signal to its characteristic fluctuations also scales as $\sqrt{\overline{N}}$ and becomes more favourable at higher photon counts[4,5]. Camera pixels have a finite capacity, often necessitating summing over many camera frames to reach a sufficiently large N and high SNR. This constraint, in turn, couples the speed of detection to the achievable sensitivity.

Detection sensitivity. The iSCAT contrast can be increased if the strength of $\mathbf{E}_{\mathrm{ref}}$ (or equivalently of r) is decreased (equation (4)). However, at the shot noise limit, the SNR remains independent of r. The signal that carries the information about the nano-object scales as $2|\mathbf{E}_{\mathrm{sca}}||\mathbf{E}_{\mathrm{ref}}|\cos\varphi \propto rs\,|\mathbf{E}_{\mathrm{inc}}|^2$ and is thus proportional to $rs\overline{N}$ if we take $\overline{N}$ to be the average number of photons in the incident beam per detection time. Moreover, the fluctuations in the detected signal (σ_{det}) are dominated by the fluctuations of the reference intensity $|r\mathbf{E}_{\mathrm{inc}}|^2$, which is equivalent to $\sigma_{\mathrm{det}} = r\sqrt{\overline{N}}$. The resulting SNR in the measured contrast C (equation (4)) thus becomes proportional to $s\sqrt{\overline{N}}$ (ref. 22). This proportionality dictates that the only way to improve the shot-noise-limited SNR is to increase the scattering cross section, the power of the incident light or the measurement integration time.

In practice, the detectors have a limited well depth and digitization resolution, making it difficult to reach the shot noise limit of the light source. Increasing C, for example by reducing $\mathbf{E}_{\mathrm{ref}}$, can help to achieve a high SNR because it effectively magnifies the number of bits that store the signal. However, beyond a certain point, reducing the reference field diminishes the iSCAT interference signal below the direct scattering intensity[22]. At that point, the detected scattering signal approaches that observed in dark-field microscopy.

Adjusting the contrast. Variations in the strength of the reference field in different schemes directly affect the iSCAT signal contrast, which can have implications in terms of the choice of camera and detection limit. The contrast C can be most easily adjusted if one employs an external independent reference field[75], but this comes at the cost of introducing a phase between $\mathbf{E}_{\mathrm{sca}}$ and $\mathbf{E}_{\mathrm{ref}}$, which must then be stabilized. In reflection iSCAT, the reference field amplitude can be reduced by adjusting the reflectivity of the interface between the substrate and the buffer solution, for example, by applying an antireflection coating to the substrate[76]. Alternatively, a portion of the reference light in the Fourier plane of the collection optics can be masked[77–79]. In the case of a wide-field illumination, the angular spread of the reflected beam is very small so that this light is focused to a point in the Fourier plane, whereas the light scattered by a nano-object has a large angular spread. Indeed, for particles at an interface with a large difference in refractive index, a substantial fraction of the scattered light captured by high-numerical-aperture microscope objectives falls at angles near the critical angle[80,81]. Thus, placing a small-radius circular beam block on the optical axis can reduce $|\mathbf{E}_{\mathrm{ref}}|$ while affecting $\mathbf{E}_{\mathrm{sca}}$ only minimally[77–79]. This scheme can also be implemented in transmission[82].

Reducing r not only increases the contrast of the signal of choice but also increases the contrast of the speckled background that originates from the sample features[5]. This can be advantageous in practice, as it allows one to visualize the glass–sample interface directly, thus aiding the adjustment of the microscope focus. Following equation 3, a 100-fold attenuation of the reflected light intensity would increase the optical contrast by 10-fold, as confirmed experimentally[77,78]. The iSCAT contrast can also be tuned by exploiting an engineered sample substrate that selectively amplifies the scattered signal through near-field photonic resonances[83].

The role of phase

Rayleigh scattering is considered to be an instantaneous process and the phase of $\mathbf{E}_{\mathrm{sca}}$ is expected to be the same as that of $\mathbf{E}_{\mathrm{inc}}$. However, $\mathbf{E}_{\mathrm{sca}}$ can experience a phase shift relative to $\mathbf{E}_{\mathrm{inc}}$ through the imaginary part of the polarizability α, which is determined by the resonances in the particle material (Box 2). Various other phenomena can also affect the phase difference between $\mathbf{E}_{\mathrm{sca}}$ and $\mathbf{E}_{\mathrm{ref}}$. For example, the reference field might experience a phase shift upon reflection from the sample substrate or other optical elements. In some arrangements such as in reflection mode, variations in the axial position of the particle introduces an oscillating travelling phase. As shown in equation (4), this phase difference directly influences the contrast. The phase of the scattering field can be measured through quantitative phase imaging approaches, such as holographic interferometry[47,84], quadriwave lateral shearing interferometry[84] or quadrature interferometry[85], which use a calibration procedure. Phase measurements provide information about the complex scattering field, although they come with the cost of implementing additional elements in the optical set-up and more complex data analysis.

Data handling

Experimental control and data acquisition complexity varies in an iSCAT experiment depending on the sample, implementation of background subtraction and acquisition speed. Typical raw iSCAT data consist of a series of recorded video frames; for recording frame rates up to a few kilohertz, the data can be transferred from the camera to a computer in real time. Cameras with higher frame rates often have intermediary storage, which can be filled very quickly and require longer time frames for data transfer.

Results

Here, we discuss the central features of iSCAT microscopy that allow one to characterize nano-objects. We emphasize the fundamentals of imaging and image processing that allow one to gain insight into

the 3D trajectory of a nano-object with exquisite spatial and temporal resolution, to determine its size and refractive index and the conditions for reaching single-protein sensitivity.

Interferometric point spread function

A central notion in microscopy is that of the point spread function (PSF), which is defined as the image of a point-like object in the optical system at work. The PSF in fluorescence microscopy is formed by $|\mathbf{E}_{obj}|^2$ and follows an Airy function, which results from the diffraction of light from the edges of an aperture; in practice, this defines the size of the microscope objective. The interferometric PSF (iPSF), however, is generated by the interference of $\mathbf{E}_{ref}$ with $\mathbf{E}_{sca}$. In general, the two fields have different wavefronts, determined by the illumination and detection schemes, leading to different iPSFs.

In wide-field iSCAT, $\mathbf{E}_{ref}$ is a quasi-collimated beam with a small width and thus experiences negligible diffraction at the objective edges. $\mathbf{E}_{sca}$, on the other hand, is a quasi-spherical wave and is diffracted by the aperture of the microscope objective. The outer rings of the resulting iPSF are therefore stronger than the commonly known Airy rings formed in an intensity image because an electric field decays more slowly than its magnitude squared value. In the case of confocal iSCAT microscopy, both $\mathbf{E}_{ref}$ and $\mathbf{E}_{sca}$ can be roughly approximated by spherical waves. Both fields experience a comparable degree of diffraction, minimizing the extent of the iPSF rings and thus becoming more comparable to that of a conventional intensity PSF[41].

The phase between $\mathbf{E}_{ref}$ and $\mathbf{E}_{sca}$ affects the detected contrast. Figure 1i shows the sensitivity of the iPSF to phase with the example of wide-field iPSFs for various microscope objective positions when a nanoparticle is placed at different axial positions. In addition, Fig. 1j emphasizes the strong modulation of the recorded iSCAT contrast in the axial direction. Microscope objectives are corrected for various aberrations, including spherical aberration. The correction is, however, carried out for the interface between the sample and the cover glass. Quantitative imaging of structures located at greater heights above this interface requires a proper consideration of this residual aberration, which is a known effect in fluorescence microscopy[86,87]. In the case of iSCAT, the residual spherical aberration results in a substantial axial asymmetry of the iPSF apparent in Fig. 1i and introduces a characteristic signature, which can be exploited to gain more information about the axial position of a nanoparticle[28,88,89]. The iPSF can also be modified by adding a phase mask in the back focal plane of the microscope objective through which the spatial phase pattern of $\mathbf{E}_{sca}$ is modulated. As an example, a spiral phase modulation effectively encodes the axial position of a particle into the shape of iPSF, which enhances the robustness in single-particle 3D localization[90]. Depending on the problem at hand, iPSFs can be computed analytically[88] or numerically[91], as well as with the support of open-source software[91,92].

Signal processing

A central challenge for iSCAT imaging of nanoscopic entities is to decipher a small signal on top of a much larger background generated by I_{ref}. A large body of applications so far have investigated particle binding to, motion along or unbinding from a surface, such as a cover glass or a biological membrane[25,27,28,34,36,50,93]. The high sensitivity of iSCAT carries the consequence that very small roughness and refractive index variations appear as a speckle-like background[31,94,95]. For common microscope cover glass, the root mean squared contrast change in the resulting speckle-like landscape can typically be as large as 1% (Fig. 2a). This can be improved by using atomically flat surfaces such as mica, but in practice, a certain degree of inhomogeneity remains, making it difficult to identify objects that generate signals of similar or smaller magnitude in a stationary image[22,96].

The desired signal and the fluctuating background have the same physical origin — scattering. Standard lock-in detection schemes, in which the amplitude, frequency or position of the illumination beam is modulated, do not help in discriminating the signal from the background unless the phenomenon of interest has features distinguishing it from the environment. An example is the exploitation of the spectroscopic resonance of plasmonic nanoparticles in a dielectric environment, such as by modulating the illumination wavelength[96]. Resonances in quantum emitters such as molecules can also be used[33], as well as the sensitivity of the particle of interest to an external electric field[97,98]. In many cases, the temporal signature of the particle of interest provides the additional information needed to distinguish it from the background, such as, for example, a virus or GNP-labelled diffusing lipids in a synthetic bilayer[24,50,99], a GNP tethered to a transmembrane protein diffusing in the plasma membrane of a live cell[28], unlabelled proteins landing on a substrate[34,35] and assembly or disassembly of structures such as viruses or microtubules[100]. If the time required for achieving a satisfactory SNR is shorter than the temporal window during which an event takes place, the process can be approximated by a static process.

Several strategies have been used to tackle different dynamic processes. In some applications, it is possible to first image the sample without the particle under study. In this case, the background can be accounted for through subtraction or division of video frames[34,36]. If the SNR is not sufficiently high in a single frame, frame binning is applied. Where prior knowledge of the background is not possible but the background signal does not change over the duration of the dynamic phenomenon under study, such as in the case of diffusion of a nanoparticle, a temporal median filter can be applied[24,35,101] (Fig. 2b). Here, the median of the contrast for each pixel is computed over a certain temporal window to establish a background image. Considering that the median value of a fluctuating signal pinpoints the most prevalent signal level, the median filter closely approximates the value corresponding to the background if the temporal window of the median filter is considerably larger than the nanoparticle dwell time within one diffraction-limited spot. By subtracting the outcome from a given frame, the footprint of the nanoparticle in that frame can be visualized. In another scenario, where a nanoparticle is detected as it binds to the surface of the sensor, the diffusive mobility of the unbound particle is high enough to average its signal within an observation interval; however, as the particle becomes confined, a subtle step-like modulation in the scattering contrast is obtained[50]. To achieve a sufficient SNR in detecting each binding event, a running average over a batch of a suitable number of frames captures the build-up of the contrast for signals that are not detectable in a single frame[34,36,69]. Consecutive frame batches are subtracted from or divided by each other to identify the weak contrast over residual speckle-like background fluctuations (Fig. 2c).

In more complex applications, the dynamics of the background may hinder a simple differential analysis[5,28]. The application of sophisticated algorithms tailored to the properties of the signal and background can, nevertheless, help to identify nano-objects. For example, sparse in time affine registration was used to mask the background stemming from the body of giant unilamellar vesicles (GUVs) when tracking GUV-attached GNPs[25] or lipid nanoparticles[102]. This approach takes advantage of the fact that the GUV background has a well-defined pattern akin to Newton rings produced by the interference of light

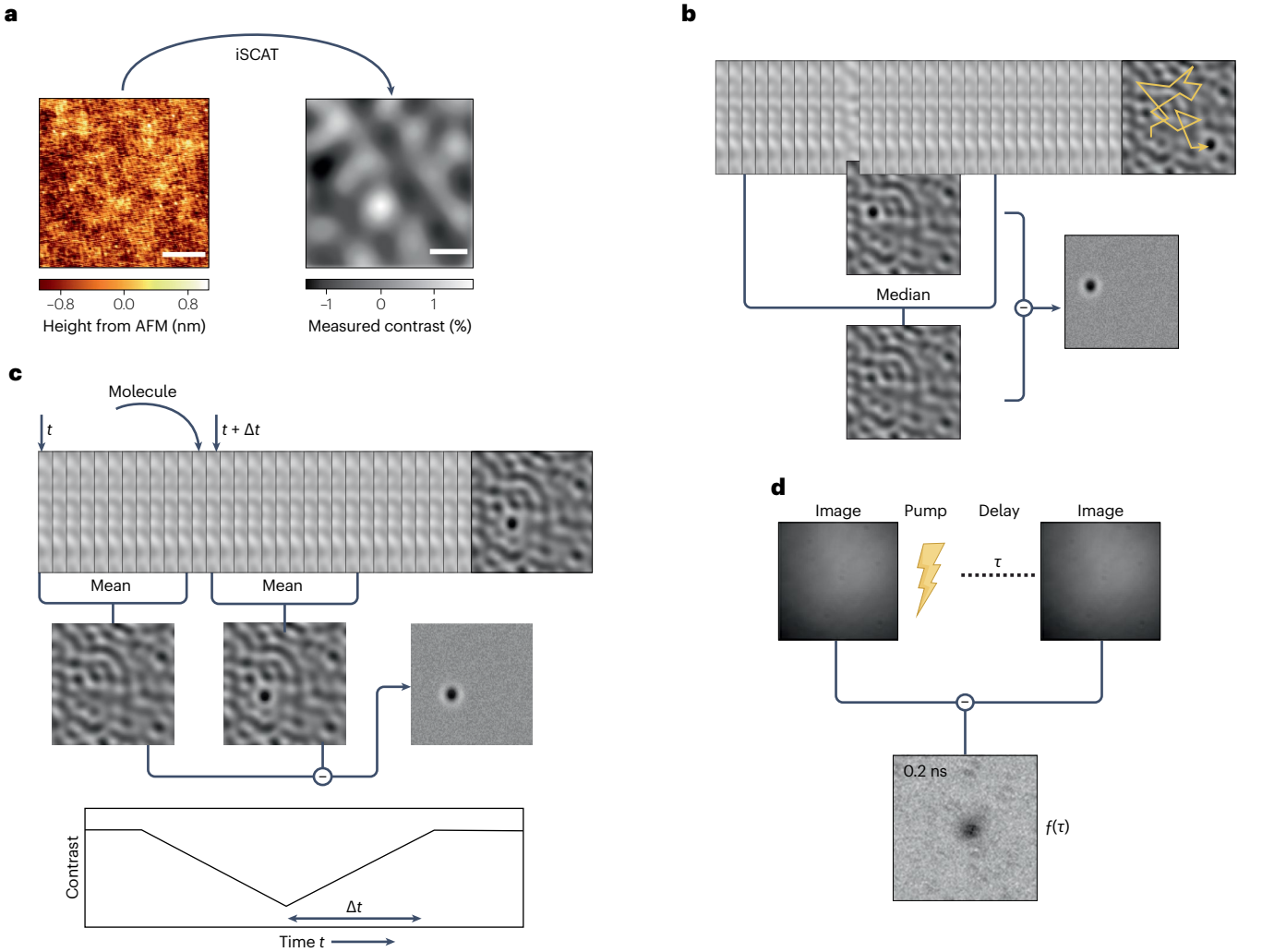

Fig. 2 | Image background and elimination. a, An atomic force microscopy (AFM) topographic image of the surface of a microscope cover glass (left) and the interferometric scattering (iSCAT) contrast image (right) of the same area measured at a wavelength of 545 nm. Scale bar, 500 nm. **b**, Temporal median filtering, where each frame is flattened by subtracting the median of surrounding frames within a defined interval. This process effectively removes static speckles and enhances the visibility of dynamic fluctuations such as diffusing particles. **c**, Differential rolling averaging of the iSCAT contrast. This technique averages batches of a certain number of frames over time interval Δt and compares these by subtraction or division as the centre of the batch is shifted in time. Deposition of a protein at the position of a given pixel results in a V-shaped signal spread over $2\Delta t$. **d**, The differential data visualization process in stroboscopic iSCAT (stroboSCAT) imaging. The subtraction of two frames, only the first of which is prepared with a confocal pump laser pulse, provides access to light-induced changes in the sample as a function of time delay τ. Panel **a** reprinted with permission from ref. 94, APS.

reflecting from a curved and a flat surface[4,25]. The motion of a GNP was also tracked on the strong dynamic speckle-like background of a biological cell using the ring-like features of the iPSF; the iPSF was first pinpointed in one frame, where its signal was clearly visible above the background, and then further used to identify the iPSF of the same GNP in neighbouring frames through a cross-correlation algorithm[28]. The spatiotemporal signature of the iSCAT signal can also establish crucial information for machine-learning algorithms to distinguish a desired event from the background[103].

When the dynamics of the system are too fast, conventional imaging is no longer sufficient. The concept for stroboscopic iSCAT (stroboSCAT) — an imaging technique for capturing ultrafast dynamics of materials — was introduced in 2018 in a preprint of a paper by Delor and colleagues[37]. StroboSCAT uses laser pulses to investigate photogenerated energy transport in solid materials[37,66]. Rather than subtracting consecutive frames under the same illumination conditions, stroboSCAT compares an iSCAT image recorded after the sample is excited by a short excitation pulse of light with an iSCAT image taken without any prior excitation pulse (Fig. 2d). Whereas both images can show heterogeneities in the structure of the material, these features are subtracted away in the differencing scheme to isolate signatures specific to a localized population of photoexcited species. By iteratively collecting such images with progressively longer time delays between the excitation pulse and the iSCAT measurement, a movie can be reconstructed to depict the spatiotemporal evolution of this population of energy carriers.

Particle tracking

Particle tracking is a powerful technique for studying individual nanoparticles and single molecules[104]. If a nanoparticle can be imaged over the background, its position can also be tracked over time. A number of images are acquired as a function of time, the particle of interest is picked in each image, and the trajectory of the particle is determined. Given that nanoparticles generally exhibit high diffusion coefficients, balancing temporal and spatial precision can pose a fundamental challenge. Technical details of single-particle tracking concerning sensitivity, precision, accuracy and speed have been extensively studied and reported over the past three decades[25,27,104]. Here we discuss the use of scattering-based methods for particle tracking, which are not limited by the saturation of the signal, allowing for shorter integration times than in fluorescence measurements. The interferometric nature of iSCAT imaging also provides crucial advantages for 3D tracking. In addition, not being affected by photobleaching, iSCAT microscopy makes it possible to track a given nanoparticle for nearly indefinite periods of time.

The simplest approach to 2D localization of a particle in iSCAT microscopy is to fit a Gaussian function to the central lobe of the iPSF[24,49,50,69,101] (Fig. 1h). Particle localization, however, becomes more efficient and robust when taking into account the radial symmetry of iPSF rings[105]. The rich features of the iPSF also carry information about the axial position of the particle[88]. First, the amplitude of the central iPSF lobe is directly affected by the travelling phase between the reference and the scattered field, reporting on the axial displacement of the particle[72,106]. The periodic behaviour of the travelling phase, however, results in a certain level of ambiguity and limits the applicability to a fraction of the wavelength of light in the medium of interest[27,106]. One approach for avoiding this complication is to exploit the Gouy phase in transmission experiments, albeit with less sensitivity than from the travelling phase[26] (Box 1). When focusing away from the microscope cover-glass interface, the residual spherical aberration of the objective is enhanced, breaking the axial symmetry of the iPSF and thereby minimizing the periodic phase limitation of the reflection configuration[28,88] (Fig. 1i). This approach to axial localization was used in the example shown in Fig. 3a, where a 40-nm GNP attached to membrane proteins in a live cell was tracked in 3D[107].

The information content of the rings and their contrasts in the iPSF provide a convenient means to track nanoparticles over a large range of several micrometres. This scheme is inherently similar to the recent advances in PSF engineering for fluorescence particle tracking[108], as the phase and wavefront information that is encoded in the iPSF render a non-trivial axial signature to it. Figure 3b shows an example in which iPSF information was used to track a 40-nm diameter GNP over a

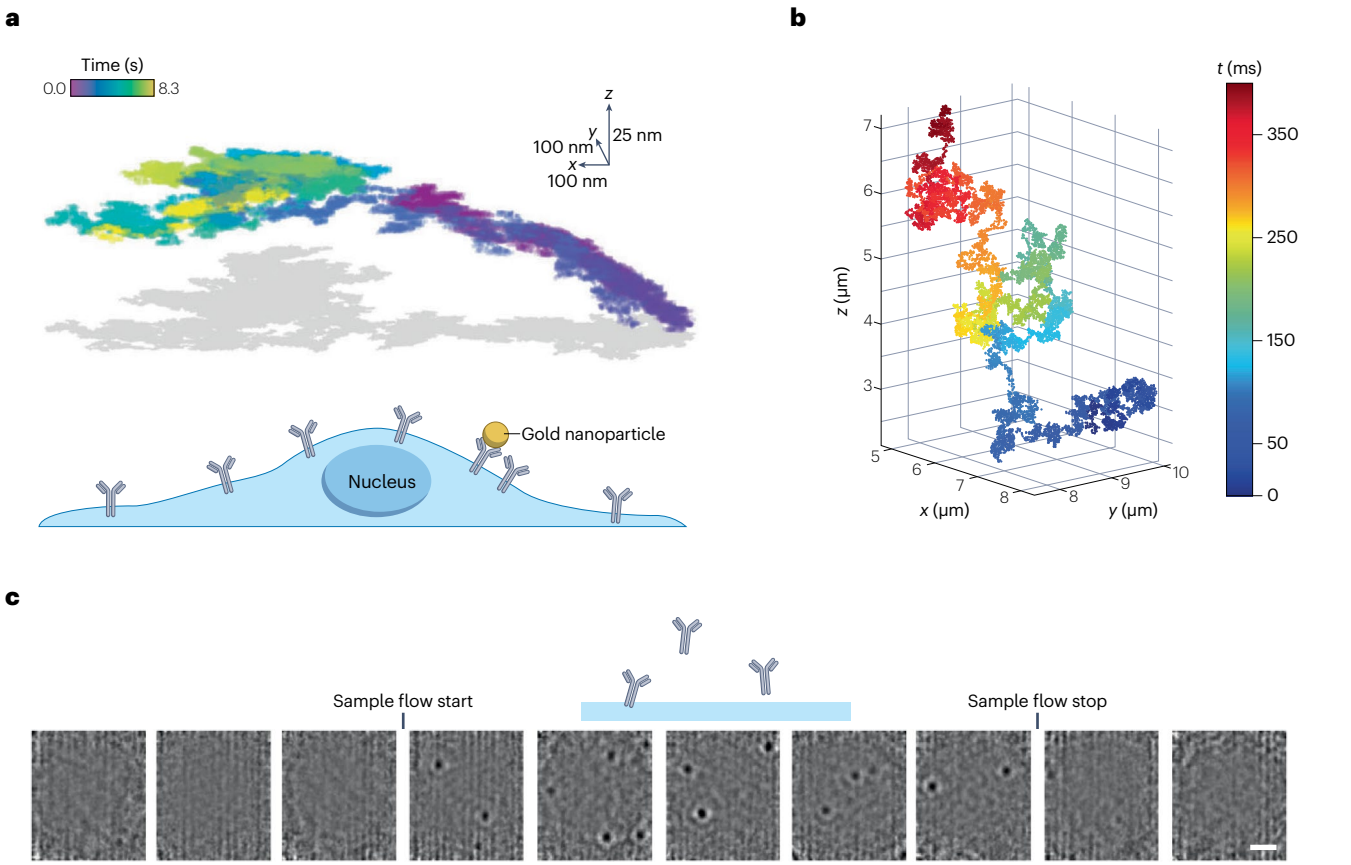

Fig. 3 | iSCAT for 3D tracking of individual nanoparticles. a, A 3D trajectory of a 40-nm gold particle bound to a transmembrane protein at the plasma membrane of a live cell. The colours denote the temporal evolution of the trajectory. The grey area shows the 2D projection of the trajectory. **b**, A 3D trajectory of a 40-nm gold particle diffusing in water over a large axial span of several micrometres. **c**, The stills of a video recorded from proteins introduced to a buffer. As each protein lands on the substrate, its interferometric scattering (iSCAT) footprint can be obtained and used to both count and localize individual proteins. The iSCAT contrast obtained from each protein reports on its mass. Scale bar, 1 μm. Panel **a** adapted from ref. 107, CC BY 4.0. Panel **b** reprinted from ref. 89, CC BY 4.0. Panel **c** adapted from ref. 34, Springer Nature Limited.

displacement of more than 10 µm (ref. 89). Engineering of the iPSF has recently been achieved[90] and promises to aid in 3D tracking. Particle localization is typically conducted through least-squares fitting of the experimental image data with the model. Correlation-based[89] and Bayesian[109] analyses improve the efficiency and accuracy of 3D particle tracking. Ultimately, the localization precision depends on the number of signal photons captured within the iPSF[90,110].

Although the SNR and thus the temporal resolution can, in principle, be indefinitely improved by increasing the incident power density, sample damage and finite camera frame rates produce realistic limitations[107,111]. Moreover, when performing fast tracking with nanometre localization precision, the intrinsic degree of label mobility should be taken into account[112]. For example, a freely diffusing 20-nm particle that is attached to a biomolecule may displace by as much as 300 nm within 1 ms. If its motion is confined by a flexible 10-nm linker, the calculated location would approximate that of the biomolecule if the integration time is as long as 1 ms. The situation is quite different when using a shorter exposure time, such as 1 µs, where the particle would only diffuse by about 10 nm in this interval. If the linker is flexible and is not substantially shorter, particle localization would essentially report on its fluctuation and not the position of the biomolecule.

Nanoparticle size and refractive index

The iSCAT contrast encodes information about the polarizability of the nanoparticle under study[22], reporting on its size[113,114], shape[29], orientation[115] and refractive index[113,114,116] (Box 2). In general, this multitude of quantities makes it impossible to determine all particle features from one single measurement. Nevertheless, prior knowledge of some of these parameters provides insight about the others, particularly in comparative studies. For example, if the material properties of the particle are known, the size distribution can be extracted from the distribution of the iSCAT contrast values[54,117]. Further, the real and imaginary parts of GNPs have been measured over a large spectral range[116]. The performance of such measurements is limited by various experimental factors such as sensitivity and speed.

Aside from polarizability, other parameters such as the strength of the reference beam and the axial position of the particle affect the observed iSCAT contrast, making it important to calibrate this quantity. To calibrate the contrast for a given set-up, a sample with known particle properties is required. This simple-seeming task is, however, non-trivial because it is difficult to fabricate nanoparticles with a very high degree of reproducibility. In practice, the features of a large number of individual particles are determined, establishing a histogram, which is then analysed to assess statistical quantities such as mean value and standard deviation[113].

Single-protein sensing and sizing

Proteins and large biomolecules usually absorb in the ultraviolet range and can thus be treated as dielectric nanoparticles with respect to their interaction with light in the visible spectrum[70]. However, assuming a typical refractive index of ~1.45 for biological matter, the scattering cross section of a small protein such as albumin is as small as 10^{-19} cm^2 (ref. 34). As a result, optical detection of proteins is usually achieved through fluorescence labelling at the single-protein level or in ensembles via absorption spectroscopy or surface plasmon resonance sensing.

In a typical sensing experiment, molecules diffuse in solution and are detected when they land on a transducer substrate (Fig. 3c). For single-molecule sensing to be possible in this arrangement, subsequent molecules should not spatially overlap within a diffraction-limited spot within the average detection time. As sensitivity was improved, single proteins became detectable through iSCAT[34,35] and proteins as small as 65 kDa were detected[34]. In addition, it was pointed out that the iSCAT contrast scales linearly with the protein mass[34,35].

Single proteins have a small iSCAT contrast, which means they cannot be detected in a single frame[34,36,69]. To address this, differential rolling averaging was implemented to integrate a sufficient number of frames to reach a SNR close to the shot noise limit[34] (Fig. 2c), and machine-learning algorithms have been exploited to push the detection sensitivity below 10 kDa (ref. 103). Recently, other experimental arrangements of iSCAT have also reached single-protein sensitivity; for example, illumination and detection via surface plasmons have been successfully used[52], molecules diffusing in strongly confined nanoscopic channels have been detected[74], and single-protein sensitivity was demonstrated in a holographic approach using an external reference beam[47].

Single-protein sensitivity in iSCAT detection was used to monitor real-time secretion from a single cell; in this study, the histogram of the measured iSCAT contrasts represented the variation of mass in the secreted proteins[118]. Accurate measurement of protein mass was demonstrated by maximizing the single-molecule measurement precision[36], enabling the analysis, identification and quantification of biomolecular mixtures at the single-molecule level in solution. This marked the advent of 'mass photometry', which has been commercialized and is used across academia and industry to study a range of biomolecular phenomena, such as self-assembly[119], interaction strengths[120] or oligomerization[121], as well as application to various biomolecules[122] and environments[101,123].

Applications

In the previous sections, we discussed various aspects of iSCAT microscopy, considering the recorded PSF and contrast, which allow determination of the 3D location of a nanoparticle and acquisition of information about its size, refractive index, shape and mass. Here, we present a few specific laboratory applications that have emerged in the past decade.

Determining size and refractive index

Knowledge of nanoparticle features such as size, shape and material in suspension is highly desirable for many applications in chemistry and pharmaceutics. Optical methods are particularly useful in these endeavours because they are rapid and non-invasive. Dynamic light scattering, based on ensemble measurements, is commonly used. A more recent solution uses nanoparticle tracking analysis (NTA) based on the dark-field microscopy of individual nanoparticles diffusing in a liquid. By extracting a diffusion coefficient from the recorded trajectory as well as using prior knowledge of the temperature and viscosity of the medium, the hydrodynamic diameter d of the particle can be determined. Dark-field microscopy measures the scattered intensity $|\mathbf{E}_{sca}|^2$, which is proportional to the square of the polarizability $|\alpha|^2$ and thus to d^6. This strong size dependence makes it challenging for NTA to analyse suspensions of particles with a wide range of sizes because the signal from the larger particles is orders of magnitude stronger than the signal from smaller ones. This challenge was recently overcome by combining iSCAT detection with NTA to give rise to interferometric NTA (iNTA)[113].

The ability of iSCAT to detect smaller particles and to access faster imaging leads to a better performance in extracting the diffusion constant of individual trajectories[113]. The combination of the extracted particle size from diffusion with the third root of the observed iSCAT

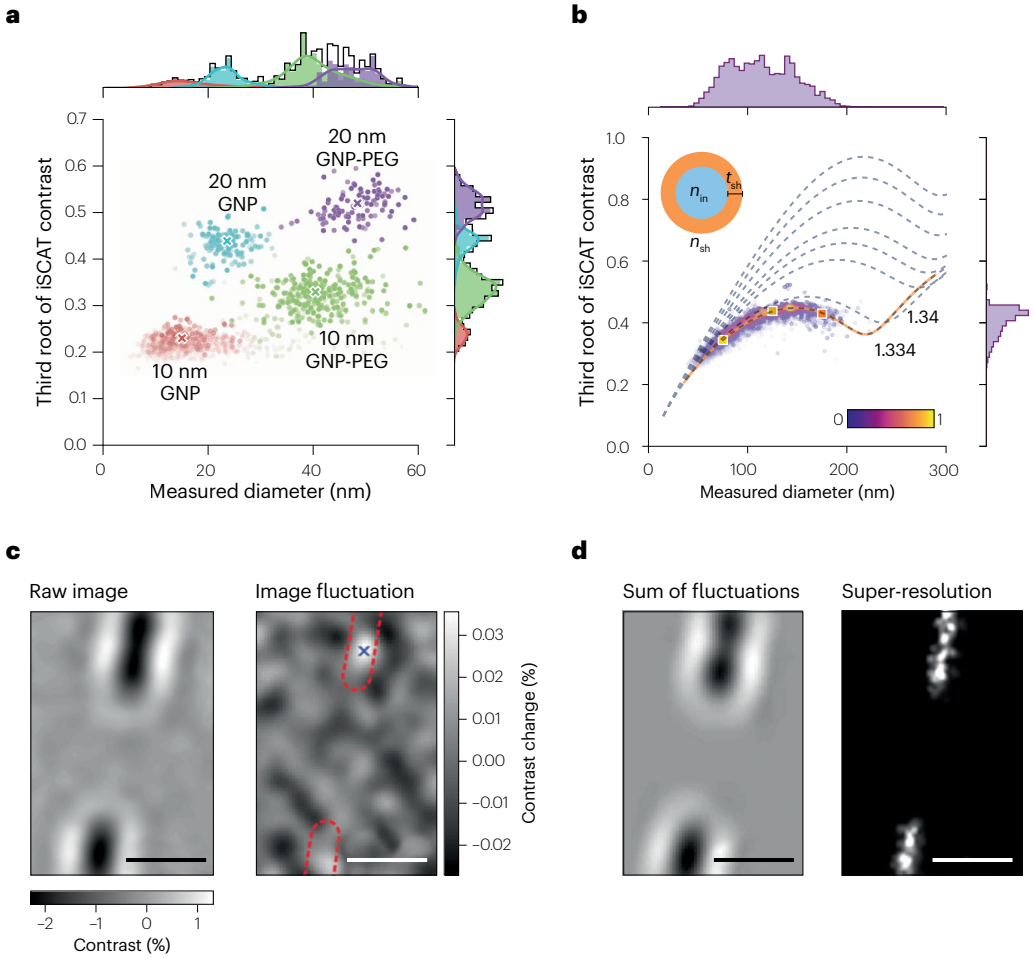

Fig. 4 | Sensitive analysis of size of nanoparticles and dynamics of protein assembly. a, Interferometric nanoparticle tracking analysis for a suspension containing a mixture of 10-nm and 20-nm gold nanoparticles (GNPs) as well as populations of particles covered with polyethylene glycol (PEG). The values on the horizontal axis show the particle diameter obtained from the diffusion trajectories and the Einstein–Stokes equation; the values of the vertical axis present the third root of the measured interferometric scattering (iSCAT) contrast, which is proportional to the particle diameter. The histograms on the right and top show the projections of the data clouds from the 2D scatter plot. **b**, The third root of the iSCAT contrast obtained from synthetically produced lipid vesicles (inset) as a function of their size distribution extracted from diffusion trajectories. The colour code indicates the normalized density of data points. The dashed lines indicate the calculated behaviour assuming different indices of refraction for the vesicle interior n_{in} in steps of 0.02, starting with 1.334 for water. The calculations assume 1.48 and 5.7 nm for the refractive index n_{sh} and thickness of the lipid shell t_{sh}, respectively. **c**, An iSCAT image of two disassembling ends of a microtubule (left) and an example of an incremental image with the detected diffraction-limited fluctuation caused by the loss of mass due to tubulin depolymerization (right). **d**, The sum of all detected fluctuations due to depolymerizing proteins and super-resolution image rendered from their localizations. Scale bars, 1 µm. Panel **a** reprinted from ref. 113, Springer Nature Limited. Panel **b** adapted from ref. 125, CC BY 4.0. Panels **c** and **d** reprinted with permission from ref. 29, Wiley.

contrast provides two independent measures that can be presented in a 2D scatter plot (Fig. 4a). This provides a more robust separation of different species in a suspension. Interferometric characterization of particles has been previously reported under the heading of digital or video holography performed in transmission[46,124]. These measurements did not reach high enough sensitivity to detect very small nanoparticles and are mostly dedicated to particles with diameters >100 nm. Recent works have improved on earlier results, extending to particles in the range of 40 nm (ref. 114).

If the size of the particle is extracted from its diffusion behaviour, its iSCAT contrast can be used to learn about its refractive index[125]. Where some prior knowledge of the particle constitution exists, such as with the core–shell structure of extracellular vesicles, quantitative information about the refractive indices and thickness of the core and shell regions can also be derived[113] (Fig. 4b).

Nanoscopic assembly and dynamics

The speed and sensitivity of iSCAT makes it a highly suited tool for exploring the coordination mechanisms and dynamics of large macromolecular assemblies. Here, changes in the macromolecular arrangement within the detection volume can change the observed scattering pattern. Careful analysis of the dynamic changes in the iSCAT image

can provide valuable insight about processes such as assembly or dissociation, even when single-protein sensitivity is not accessible, such as has been captured for the dynamics of adsorption and rupture events in supported lipid bilayers involving individual vesicles[126] and lipid domain formation[127], respectively. When observing the interferometric image of specific macromolecular assemblies, it becomes feasible to pinpoint contrast fluctuations[29] and associate them with various phenomena such as the binding, unbinding, reorganization or even displacement of both labelled and unlabelled biomolecular structures. Label-free tracking was used to monitor single virus particles as they attached to supported membrane bilayer receptors[50]. Similarly, the positions and orientations of unlabelled bacteriophages were tracked with nanometre precision by monitoring iSCAT signals from the release of virion DNA content, thereby discerning DNA ejection dynamics of individual bacteriophages[128] and viral capsid assembly[129].

iSCAT microscopy has been used to study the compartmentalization of diffusion for single lipids and membrane proteins, revealing deviations from Brownian motion in raft-containing membranes on microsecond timescales[93]. Further advances in high-speed tracking of membrane proteins via scattering labels are enhancing our understanding of the complex interactions taking place on the surface of living cells, by, for example, tracking the interactions of single transmembrane protein receptors[28]. Leveraging 20-µs temporal resolution and a spatial resolution >2 nm enabled the capture and sorting of millisecond confinements aligned with the periodic tubulin lattice, rendering the energetic landscape of the interaction[130]. iSCAT studies have also demonstrated the feasibility of capturing the dynamics of microtubule polymerization from a tubulin solution, which was sparsely labelled with a 20-nm GNP[131]. During this polymerization, gold-labelled subunits were transiently bound to the growing tips of the microtubules, enabling the quantification of tubulin association and dissociation rates.

The ultimate goal is to examine these assembly or disassembly processes in a label-free manner. This can be achieved if the detection speed is sufficiently high relative to the (dis)assembly speed, and if the system possesses adequate sensitivity for label-free detection of single-biomolecule fluctuations. One example is the monitoring of disassembling microtubules at high frame rates in vitro[29]; observing the unbinding of individual tubulin oligomers approximately every few milliseconds suggests that microtubule disassembly is a discrete process, where tubulin dimers depolymerize from the microtubule tips in the form of small oligomers (Fig. 4c). These discrete depolymerizing events can be detected with high yield (~60%), and their localizations enabled the reconstruction of a super-resolution image based solely on the unlabelled single-protein fluctuations (Fig. 4d).

Label-free imaging

In addition to label-free detection and characterization of nanoparticles and molecules in sparse environments, iSCAT microscopy offers an exciting opportunity to explore complex biological samples such as live biological cells. iSCAT is particularly powerful in capturing dynamics in live cells over a wide range of timescales, whereas fluorescence-based microscopy is limited in observation time and speed, owing to photon budgets and phototoxicity. Indeed, label-free cellular imaging based on interferometric methods such as phase contrast, differential interference contrast, interference reflection microscopy[9], confocal reflection microscopy[18], quantitative phase imaging[10,132], digital holography and their variants has been a topic of research for several decades. These methods typically examine larger entities such as cells or the cell nucleus. Recent iSCAT efforts have opened the door for label-free visualization of nanoscopic cellular structures[41,42]. Moreover, long-term tracking of cell vesicles[133] and fast tracking of single virus particles in live cells have become possible by exploiting stable iSCAT signals[26] (Fig. 5a–c), and nucleation events of nascent adhesion at the basal cell membrane were observed[134]. iSCAT imaging can also be readily combined with fluorescence microscopy to benefit from the spectral specificity of fluorescence labels and thus identify different cellular features such as clathrin-coated pits, microtubules, vesicles and viruses[41].

Resolving nanoscopic cell structures is made difficult by a strong speckle-like background that results from the scattering of illumination in a dense medium, particularly when using coherent light. Non-specific cellular background in wide-field iSCAT imaging has been shown to be largely removed through image postprocessing when the target of interest and background exhibit different spatiotemporal characteristics[28,135]. It is also possible to substantially reduce the non-specific background by performing confocal iSCAT microscopy. Here, the confocal pinhole discriminates against much of the light that is scattered from the unwanted region[41]. When integrated with a spinning-disk confocal unit, an image acquisition rate of up to 1,000 Hz can be achieved[42]. Figure 5d presents an example for a confocal iSCAT image of endoplasmic reticulum in the periphery of a live mammalian cell. These are soft tubular structures with a diameter of approximately 50 nm, which are dynamically formed and are challenging to image in fluorescence microscopy. The 3D information from the iPSF facilitates analysis of the 3D contour of the tubules (Fig. 5e). In the same fashion, nanoscopic features of the surface contour of the nucleus or other extended organelles can be mapped[41]. However, 3D volumetric details of dense and crowded regions of the cell, such as the nuclear interior, cannot be directly resolved with iSCAT because the strong axial modulations of the iPSF within the diffraction limit (Fig. 1j) lead to the smearing of the iSCAT contrast[41].

A new approach to wide-field cellular imaging and particle tracking has been demonstrated in which the degree of spatial coherence of the illumination laser beam was adjusted at will[53]. A rotating diffusor in the illumination path was used to tailor the extent of the outer rings in the iPSF, enabling control of the resulting speckle in the image. iSCAT cellular imaging has also used the temporal variations of the signal to analyse the organization and dynamics of the sample within a detection volume, which was used to examine nanoscale condensation of chromatin in live cell nuclei[136].

Ultrafast imaging of excited-state energy transport

Fluorescence-free optical microscopy is also of great interest in condensed matter physics and materials science, where the distribution of nanostructures, energy carriers and other processes that manifest themselves through light–matter interaction are of interest. The high detection sensitivity of iSCAT enables the detection of minute changes in the local optical properties of solids. Imaging such entities confined to subwavelength regions constitutes the nanoscopic limit of interference reflection microscopy[9,137] (Box 3). The first application of iSCAT in this area was the detection of a single semiconductor quantum dot both at liquid helium[30] and at room temperature[31]. Recently, the DNA nanostructures on 2D materials have been detected[138].

A particularly important development in the application of iSCAT to nanoscopic solid-state phenomena has come from stroboSCAT measurements[37,65,67], which have succeeded in determining how photoexcitations in solids spatiotemporally explore the material. The photoexcitation of a semiconductor or conductor in a localized spot

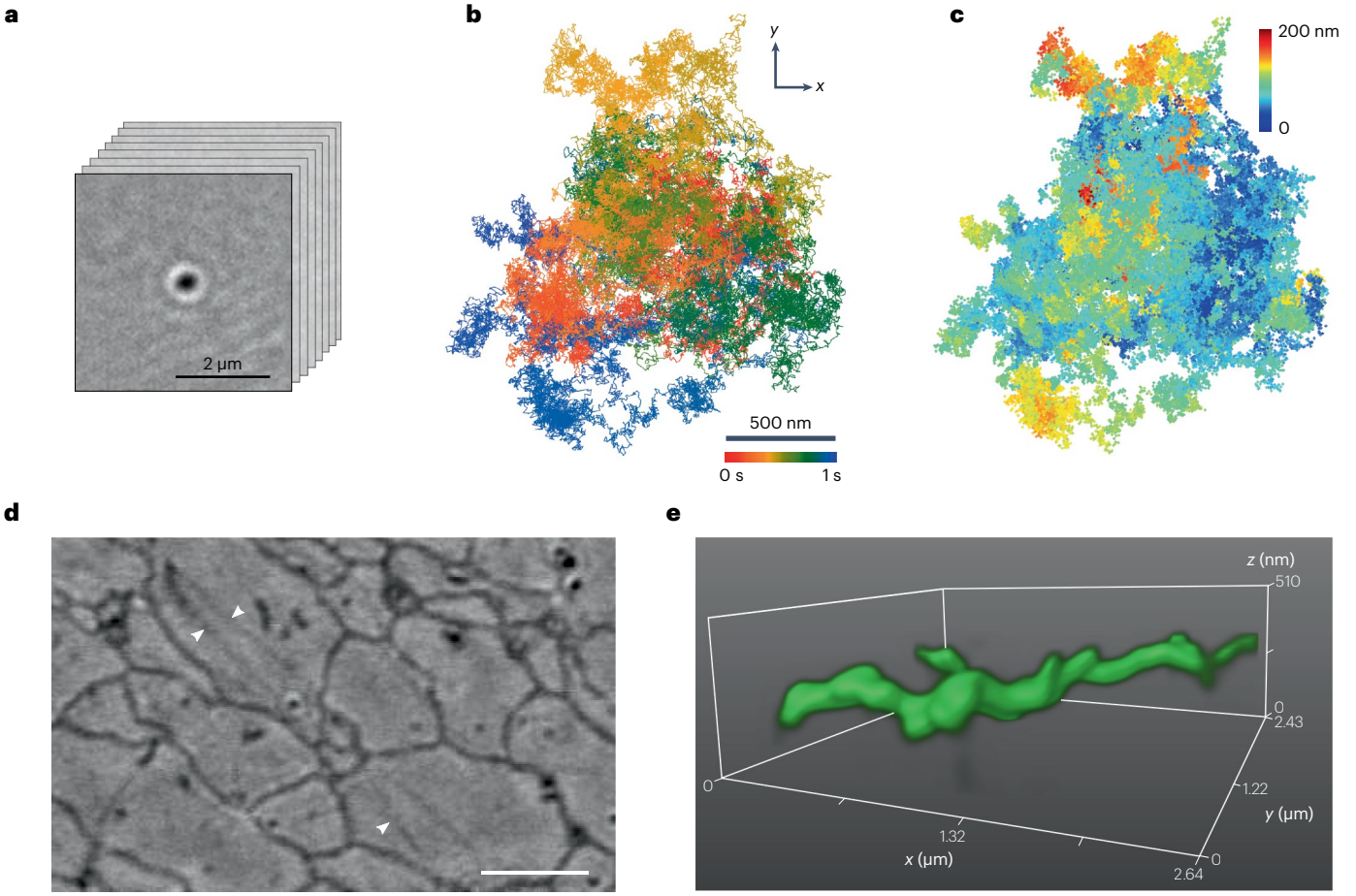

Fig. 5 | Label-free 3D nanoscopic cell imaging. a, Interferometric scattering (iSCAT) image stacks of a single vaccinia virus particle on the surface of a live cell from a video recorded at a high speed of 100 kHz, showing clear visualization of the virus particle. The relatively stationary and heterogeneous cell background was removed using temporal median filtering. **b**, The 2D trajectory of the viral particle resolves its diffusive motion on the cell surface with nanometre spatial precision. **c**, A map for the axial position of the virus in panel **b**. **d**, A confocal iSCAT image of the endoplasmic reticulum and microtubules (marked by white arrows) in a live cell. Scale bar, 2 µm. **e**, A 3D rendering of a section of an endoplasmic reticulum tubular network. Panels **a**–**c** adapted with permission from ref. 26, American Chemical Society. Panels **d** and **e** adapted from ref. 41, Springer Nature Limited.

produces populations of electronic and thermal excitations that, in turn, alter the local index of refraction relative to the unilluminated surroundings (Fig. 6). The individual energy carriers are not sparse and have mean separations well below the diffraction limit[37]. As a simple example, consider a Gaussian-distributed population of energy carriers created by a first laser pulse in a homogeneous medium. Owing to the concentration gradient of these energy carriers, their population will diffuse by frequent scattering with the nuclei in the material and possibly with one another, either until it is uniform or until these excitations relax. Therefore, at successive femtosecond-to-nanosecond time delays, iSCAT images are obtained of progressively broader Gaussian distributions whose integrated amplitude decays at the according excitation lifetime[139] (Fig. 6a,b). For an instantaneous distribution standard deviation $\sigma(t)$ and initial standard deviation σ_0, the slope of the mean squared expansion of the initial distribution, $\sigma(t)^2 - \sigma_0^2$, as a function of time delay t is proportional to the energy carrier diffusivity (Fig. 6c).

StroboSCAT imaging has been used both in the picosecond and femtosecond regimes[39,60,61,67]. The sensitivity to changes in the spatial distribution of the population can be <10 nm owing to the use of shorter optical pulses, which can more readily differentiate changes to image features formed at commensurately shorter time delays between excitation and iSCAT signal. The sensitivity of stroboSCAT can be increased with integration time at a given time delay. Leveraging a backscattering geometry increases the sensitivity to refractive index changes.

The ability to directly extract the spatiotemporal evolution of photoexcited species from stroboSCAT data is increasingly valuable in situations where the material is structurally heterogeneous. In this case, an initially Gaussian distribution evolves irregularly in either or both of space and time, and the effects of grain boundaries, voids and atomic defects each generate distinct and interpretable signatures[37,57–59,66]. For example, stroboSCAT reveals distinct differences in the evolution of the mean squared expansion of excitons in polycrystalline thin films, depending on whether they are generated at, near to or far from crystalline grain interfaces[37]. At the atomic scale, lattice vacancies may serve as traps for energy carriers[58]. In stroboSCAT, their presence often shows up as a slowed rate of mean squared expansion versus time (Fig. 6c).

At early times after photoexcitation, however, the local carrier density may initially exceed the trap density such that the higher intrinsic carrier diffusivity can be observed to identify the material's true transport capacity beneath the bulk[58].

Among forms of transient microscopies[140–144], stroboSCAT is uniquely sensitive to heat in materials owing to its sensitivity to changes in the real part of the refractive index[61] (Fig. 6d). Although these data do not show irregularities associated with structural heterogeneity, the different signs of contrast simultaneously observed at one probe wavelength show that heat and excitons can be simultaneously detected. Mindfully subtracting from these images those that isolate heat can be used to recover the exciton spatiotemporal evolution[61]. Photogenerated heat is ubiquitous, especially with ultrafast pump laser pulses, and this ability to discern it from electronic excitations with 100-mK sensitivity prevents mistaking heat for electronic energy. The capability to discern heat and charge in materials should aid the investigation of energy transduction between these two forms, which is of import both for thermal management and thermoelectric characterization.

The interferometric nature of stroboSCAT also enables out-of-plane transport to be measured[37]. The same energy carrier species may be recorded with a depth-dependent scattering phase that depends

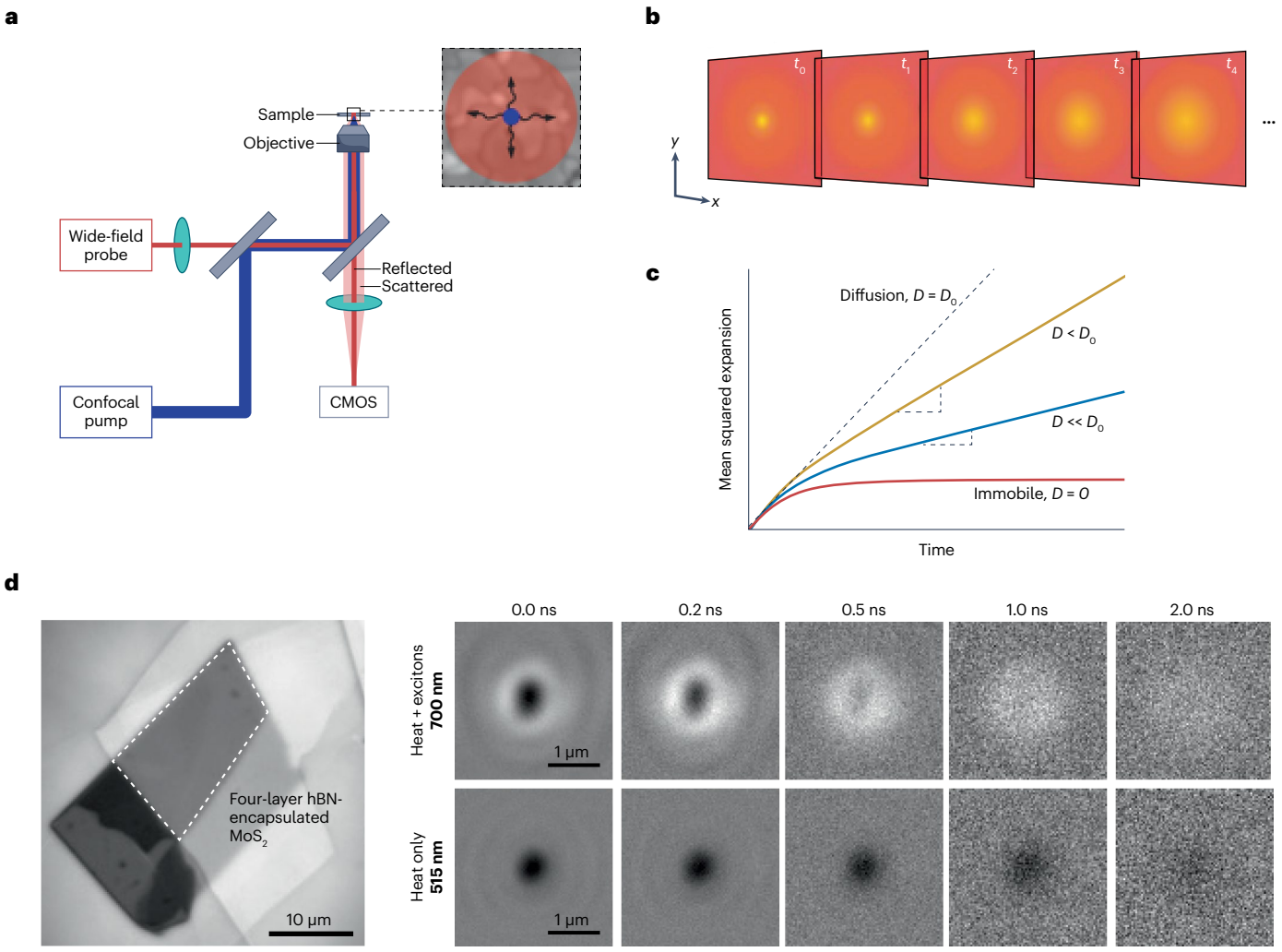

Fig. 6 | Stroboscopic energy flow microscopy in materials. a, A schematic of a typical stroboscopic interferometric scattering (stroboSCAT) experimental set-up using a confocal pump laser pulse to photoexcite a diffraction-limited population of energy carriers and a time-delayed wide-field interferometric scattering (iSCAT) probe pulse. **b**, Upon successive repetitions of the experiment for a given time delay, the pump pulse is chopped on and off so that the material response to the energy carriers can be isolated by both subtracting and normalizing with respect to the pump-off image. An example time series shows the spread of the signal. **c**, The mean squared expansion of the initial population plotted as a function of pump–probe time delay so that, in the case of normal diffusion, a diffusion coefficient can be extracted from the slope of the curve. More complex mean squared expansion plots arise in heterogeneous materials, enabling the identification of types of heterogeneity at various scales. **d**, Left: a reflection image of a four-layer MoS_2 sample encapsulated in hexagonal boron nitride (hBN), indicated by the dashed box. Right: the transport of excitons (light contrast) can be extracted from the overall stroboSCAT signal despite the presence and evolution of heat (dark contrast) in four-layer MoS_2 by relating the time series obtained when imaging at two different wavelengths of 515 and 700 nm. CMOS, complementary metal–oxide–semiconductor. Panel **a** reprinted from ref. 37, Springer Nature Limited. Panel **b** reprinted with permission from ref. 139, Annual Reviews. Panel **c** adapted with permission from ref. 58, American Chemical Society. Panel **d** adapted from ref. 61, CC BY 4.0.

on the refractive index of the material. This feature is exemplified as charge carriers cross an interface in a metal halide perovskite thin film[37]. A combination of lateral and axial transport measurements, together with in situ recorded images of the polycrystalline material structure, served to correlate the phase changes with the location of crystal grain interfaces. stroboSCAT has also revealed that by coupling to optical cavity modes, excitons can adopt ballistic behaviours in materials[62,145]. To strike a balance in these light–matter superposition states, an important additional technical capability was developed to resolve the momentum of the excitations, whereby the detected light is additionally imaged in the Fourier plane[62]. This stands to become a powerful mode of operation to enable additional materials characterization and may be useful in iSCAT experiments that are not stroboscopic.

Owing to the basic principle of detecting changes in the index of refraction, iSCAT is now enabling the resolution of dynamic processes in material assembly, chemistry at surfaces and electrochemical ion transport in solid and liquid media[55,146–151]. It has been used to resolve various surface reactions on graphene[146–148], porous materials formation[40], ion migration in battery electrodes[149–151] and other electrochemical reactions[98,152–156]. Beyond imaging alone, it has also enabled the diffusivity of electrochemical products to be correctly quantified by adapting the mean squared expansion analysis in stroboSCAT[55].

Reproducibility and data deposition

The iSCAT contrast is dependent on many experimental configuration-specific factors, complicating the quantitative reproducibility of iSCAT data. These challenges are mitigated by providing comprehensive descriptions of the experimental set-up, ideally including detailed specifications of the light source, optical components, detectors and electronics used in data acquisition. Critical features that should be clearly highlighted include wavelength, power, polarization, instrumental noise, coherence length and mode structure of the light source; polarization of the incident light at the sample; dark noise, the dynamic range, the full well capacity, linearity and pixel size of the detectors; numerical aperture and the total magnification factor of the imaging system; any custom optical elements involved in the set-up; image acquisition speed and any means of synchronization or triggering; and image processing algorithms. In addition, the approaches used to reduce measurement noise, such as focus tracking or focus lock mechanisms, should be stated, along with strategies for vibration and airflow reduction.

Stating detailed protocols and troubleshooting guides are particularly valuable for researchers constructing bespoke iSCAT set-ups. There are a few protocols and tutorial-type descriptions to construct an iSCAT microscope, in which detailed step-by-step procedures for alignments are described and troubleshooting is included[48,49]. Existing microscopes can also be adapted for iSCAT microscopy; for example, laser scanning and spinning disk microscopes have been successfully used[41,42].

The management of iSCAT data requires meticulous documentation of experimental protocols and computational analyses to allow careful analysis for enhancing both the SNR and signal-to-background ratio. As image processing procedures vary greatly depending on the experimental design and the iSCAT signal, it is valuable to make data and software openly available. This includes a detailed explanation of the image processing methods used for background removal and noise reduction. Open-source software, such as PiSCAT[92], can be used for executing various analyses, but the parameters used in these analyses must also be shared openly in publications to ensure reproducibility. Ideally, the effects of image processing should be evaluated and validated by exploring a range of parameters, justifying the robustness of the analysis. When applicable, the codes for image analysis and the image data set should be shared on common depositions, such as Zenodo, FigShare, BioStudies and the Image Data Resource.

The size of iSCAT data, which can include hundreds to millions of images per measurement, presents challenges for data sharing, and there are currently no standards for sharing experimental iSCAT data. Although some data sets are shared as supplementary materials in journal articles[41,100,135], a more systematic approach involves depositing both raw and processed data sets in accessible repositories to aid transparency and encourage broader validation across the scientific community.

Limitations and optimizations

The lack of material specificity in iSCAT remains a major challenge. The signals scale with the polarizability of the sample, which in turn depends on particle volume, shape and refractive index, as well as the refractive index of the surrounding medium[5]. As a result, signals from a 20-nm-diameter GNP in oil, an 80-nm-diameter silica particle in air or a 100-nm-diameter lipid vesicle in water are essentially identical. Unless a thorough polarization study is carried out[71], the combination of the illumination polarization and the object orientation can lead to different contrasts for elongated objects[157].

The coherent nature of iSCAT microscopy combined with high sensitivity leads to the omnipresence of a speckle-like background, particularly in wide-field imaging mode[53], which complicates the differentiation of a particle of interest over the modulatory background when the signal of interest is not much larger[34,158]. For time-dependent events such as diffusion or transport of nano-objects, it is possible to mask the speckle background by differential measurements as long as the event of interest is faster than any changes that might occur in the background[27,28]. Nevertheless, the unavoidable shot noise of the background prevents its perfect elimination, imposing a detection sensitivity limit.

A key challenge in iSCAT microscopy, as with any form of measurement, arises when the signal becomes comparable with the noise level. As iSCAT is inherently shot noise limited, various strategies can improve the SNR, such as longer integration time, stronger illumination and detectors with larger dynamic range. Machine-learning methods can be used to decipher small signals very close to the noise level; for example, anomaly detection[159] recently pushed the protein detection limit from around 40 kDa to below 10 kDa (ref. 103) using an algorithm that considers the speckle background to be the normal image and exploits the spatiotemporal features of the recorded iSCAT videos to identify deviations caused by protein landing events.

Another complication arises due to the signal being phase sensitive, meaning it can be modulated as the particle moves along the optical axis[72,88,106]. Although this feature is a substantial advantage for 3D particle tracking[89], it can also lead to ambiguity in dense and crowded samples because the contributions from axially neighbouring entities can give rise to opposite contrasts, thus causing a smearing effect[41].

Outlook

In its first two decades, iSCAT research focused on pushing the sensitivity limit and extending its use to various research fields. The central challenge in iSCAT studies remains the extraction of small signals of

interest from the background of a sample with spatiotemporal complexity. Being ultimately limited by shot noise, however, there is no fundamental barrier to pushing the sensitivity of iSCAT detection further in various applications. The current detection limit for proteins is 10 kDa (ref. 103), providing access to important disease markers such as cytokines. It is conceivable that this limit could be extended to 1 kDa in the future. Improvements can be ushered in through various measures, such as better camera technology for larger well capacity and more pixel homogeneity, the use of well-characterized substrates to reduce background speckle and improved data analysis for characterizing background fluctuations.

Improvements in instrumentation and data analysis will also affect the use of iSCAT in diagnostics and characterization of (bio) nanoparticles. The quantification of nanoparticles such as viruses, lipoproteins, extracellular vesicles and drug delivery vesicles is currently in high demand[160] but complicated by characterization of the size, concentration and content of these particles. Developments in 3D iSCAT tracking[89] and combination of iSCAT with fluorescence-based or Raman-based spectroscopies present a powerful approach for addressing these demands. Other technologies, such as microfluidics and nanofluidics[74,161], particle trapping approaches[162,163] and surface functionalization[164], will add to the laboratory toolbox for tackling these challenges.

iSCAT research has recently embarked on the studies of more complex samples, such as extended semiconductors or biological cells[26,41]. It is now possible to visualize small vesicles, viruses, nanoscopic filaments such as microtubules and many other entities in live cells in a label-free fashion while being fully compatible with simultaneous fluorescence imaging. The important added value of iSCAT microscopy is its ability to perform both fast and slow imaging because it does not suffer from fluorescence bleaching, blinking and saturation. This opens the door to new holistic and more sophisticated studies, allowing visualization of both small numbers of organelles that have been fluorescently labelled and various cellular events at the same time, providing insight into cooperativity in cellular function. In parallel, many groups using other interferometric techniques such as interference reflection microscopy, quantitative phase imaging and holography, which have traditionally imaged supra-wavelength entities, have pushed their limits towards smaller objects such as viruses[165]. This convergence promises to merge different communities and expertise further to tackle a broader range of applications in label-free imaging.

The spatial resolution of iSCAT microscopy is generally diffraction limited. However, just as single-molecule localization beyond the diffraction limit has been used to achieve super-resolution in fluorescence microscopy, the sensitivity of iSCAT to particles as small as single proteins allows one to localize them precisely[34,35] and thus perform a super-resolution iSCAT microscopy under certain conditions. For example, nanometric precision in the position of protein binding sites[34] and monitoring of their unbinding events[69] has been demonstrated. Implementation of other strategies used in super-resolution fluorescence microscopy, such as PAINT[166], is also promising.

Most textbook descriptions of resolution in microscopy, and particularly fluorescence microscopy, consider incoherent imaging[167]. However, discussion of resolution in iSCAT imaging is more subtle because iSCAT microscopy is inherently a coherent process. Thus, there is a need for closer scrutiny of the theoretical foundation of image formation, which would also shed light on the transitions from isolated nanoparticles to extended objects, bridging the conceptual gap between iSCAT and interference reflection microscopy (Box 3).

Glossary

Accumulation
Summing multiple measurements to improve the signal-to-noise ratio.

Airy function
A mathematical representation of the diffraction pattern created by a circular aperture.

Beam scanning mode
An imaging configuration whereby a focused beam is moved sequentially across the field of view.

Bit depth
The number of bits used in the digitalization process to encode the signal in each pixel, determining intensity resolution.

Extinction
A phenomenon in which energy is lost from a travelling beam owing to its interaction with an object.

Fresnel coefficients
Multiplicative coefficients that describe the ratio of the amplitude of an electric field of light upon reflection from and transmission through interfaces of two different materials.

Gouy phase
The phase shift experienced by a beam of light when confined in the transverse direction, as is the case for a Gaussian beam. The phase shift is strongest in the region of the focal plane.

Interference
A phenomenon in which two or more coherent waves are superposed, resulting in a wave of added amplitudes. Depending on the relative phases of each wave, the total amplitude at any given moment or location might be larger or smaller than the individual components.

Measurement integration time
The time interval over which a signal is accumulated.

Pixel well depth
The maximum number of photoelectrons that a detector pixel can accumulate before becoming saturated.

Point spread function
(PSF). A 3D intensity distribution describing the response of an imaging system to a point-like source.

Wide-field mode
An imaging configuration that captures a large area without scanning the illumination beam.

Such theoretical developments also provide a solid platform for treating high-resolution microscopy in dense scattering media.

There is also potential for iSCAT in materials science, both in solid and liquid phases. iSCAT already complements many established analytical techniques. Material formation and assembly, complex chemical reactions and energy transport all stand to benefit from the generality and sensitivity of optical scattering. As the sensitivity of detection improves, previously inaccessible features become observable. Enhanced detection speeds will permit the analysis of more complex samples at higher concentrations, providing a deeper understanding of biomolecular interactions within their native environments. The potential to capture high density biomolecular interactions in biologically relevant systems hinges on achieving sufficient detection rates and sensitivity, which poses major technical challenges for the ongoing development of iSCAT imaging in biological research. Although the spatiotemporal resolution of single-particle tracking in iSCAT experiments greatly surpasses that of fluorescence-based methods, extending into the realms of interaction displacements and timescales typical of protein–protein interactions, the experiments conducted so far have only begun to tap into the vast information

potential afforded by these advanced capabilities. Just as iSCAT stands to address increasingly complex materials and reactions, real-world emerging semiconductors and conductors often support many types of energy carrier simultaneously as they evolve, interconvert and explore the material and its heterogeneities at multiple scales. Further methodological advances will increase the complexity of scenarios that can be treated so that energy transport and transduction are properly identified and characterized.

Given the generality of Rayleigh scattering within the greater optical spectrum, iSCAT can be readily extended to the ultraviolet and infrared regions of the spectrum. However, the challenge in reaching high sensitivity levels will be posed by the performance of the optical components, detectors and cameras in each case. Extension to these spectral regimes will be particularly interesting for samples that have electronic or vibrational resonances outside of the visible spectrum[168,169]. Resonant imaging not only benefits from larger extinction cross sections but also provides a good degree of specificity and background reduction. In addition, multiwavelength measurements hold promise for a range of applications, where spectroscopic information of nano-objects or the background can be used to eliminate the latter[37,96] or to reach a better SNR.

Interferometric microscopy and sensing have been around for more than a century, and they continue to push the limits of measurements, as was recently highlighted by the detection of gravitational waves[170]. Many of the measurement strategies used for advanced interferometry can also be applied to iSCAT microscopy. These developments will extend the scope of label-free iSCAT investigations to different modalities, sensitivity and applications, just as the development of the past three decades in fluorescence microscopy have given rise to a large palette of valuable techniques such as super-resolution microscopy, structure illumination microscopy and light sheet microscopy. The combination of iSCAT-derived information with that of other measurement and manipulation techniques will provide a formidable addition to the laboratory toolbox for tackling imaging and sensing challenges.

Published online: 10 April 2025

References

1. Weisenburger, S. & Sandoghdar, V. Light microscopy: an ongoing contemporary revolution. *Contemp. Phys.* **56**, 123–143 (2015).
2. Adhikari, S. & Orrit, M. Progress and perspectives in single-molecule optical spectroscopy. *J. Chem. Phys.* **156**, 160903 (2022).
3. Mazumder, N. et al. Label-free non-linear multimodal optical microscopy — basics, development, and applications. *Front. Phys.* https://doi.org/10.3389/fphy.2019.00170 (2019).
4. Saleh, B. E. A. & Teich, M. C. (eds) *Fundamentals of Photonics* 3rd edn Vol. 1 and 2 (Wiley, 2019).
5. Taylor, R. W. & Sandoghdar, V. in *Label-Free Super-Resolution Microscopy* (ed. Astratov, V.) 25–65 (Springer, 2019).
6. Zernike, F. Phase contrast, a new method for the microscopic observation of transparent objects. *Physica* **9**, 686–698 (1942).
7. Zernike, F. Phase contrast, a new method for the microscopic observation of transparent objects part II. *Physica* **9**, 974–986 (1942).
8. Normarski, G. Dispositif oculaire a contraste de phase pour microscope. *J. Phys. Radium* **11**, 9–10 (1950).
9. Curtis, A. S. G. The mechanism of adhesion of cells to glass: a study by interference reflection microscopy. *J. Cell Biol.* **20**, 199–215 (1964).
10. Park, Y., Depeursinge, C. & Popescu, G. Quantitative phase imaging in biomedicine. *Nat. Photonics* **12**, 578–589 (2018).
11. Javidi, B. et al. Roadmap on digital holography [Invited]. *Opt. Express* **29**, 35078–35118 (2021).
12. Lane, N. The unseen world: reflections on Leeuwenhoek (1677) 'Concerning little animals'. *Philos. Trans. R. Soc. B* **370**, 20140344 (2015).
13. Cocquyt, T., Zhou, Z., Plomp, J. & van Eijck, L. Neutron tomography of Van Leeuwenhoek's microscopes. *Sci. Adv.* **7**, eabf2402 (2021).
14. Mie, G. Beiträge zur Optik trüber Medien, speziell kolloidaler Metallösungen. *Ann. Phys.* **330**, 377–445 (1908).
15. Zimm, B. H. Apparatus and methods for measurement and interpretation of the angular variation of light scattering; preliminary results on polystyrene solutions. *J. Chem. Phys.* **16**, 1099–1116 (1948).
16. Thompson, B. J. & Zinky, W. R. Holographic detection of submicron particles. *Appl. Opt.* **7**, 2426–2428 (1968).
17. Batchelder, J. S. & Taubenblatt, M. A. Interferometric detection of forward scattered light from small particles. *Appl. Phys. Lett.* **55**, 215–217 (1989).
18. Amos, L. A. & Amos, W. B. The bending of sliding microtubules imaged by confocal light microscopy and negative stain electron microscopy. *J. Cell Sci.* **1991**, 95–101 (1991).
19. Kalkbrenner, T., Ramstein, M., Mlynek, J. & Sandoghdar, V. A single gold particle as a probe for apertureless scanning near-field optical microscopy. *J. Microsc.* **202**, 72–76 (2001).
20. Klar, T. et al. Surface-plasmon resonances in single metallic nanoparticles. *Phys. Rev. Lett.* **80**, 4249–4252 (1998).
21. Boyer, D., Tamarat, P., Maali, A., Lounis, B. & Orrit, M. Photothermal imaging of nanometer-sized metal particles among scatterers. *Science* **297**, 1160–1163 (2002).
22. Lindfors, K., Kalkbrenner, T., Stoller, P. & Sandoghdar, V. Detection and spectroscopy of gold nanoparticles using supercontinuum white light confocal microscopy. *Phys. Rev. Lett.* **93**, 037401 (2004).
23. Arbouet, A. et al. Direct measurement of the single-metal-cluster optical absorption. *Phys. Rev. Lett.* **93**, 127401 (2004).
24. Hsieh, C.-L., Spindler, S., Ehrig, J. & Sandoghdar, V. Tracking single particles on supported lipid membranes: multimobility diffusion and nanoscopic confinement. *J. Phys. Chem. B* **118**, 1545–1554 (2014).
25. Spindler, S. et al. Visualization of lipids and proteins at high spatial and temporal resolution via interferometric scattering (iSCAT) microscopy. *J. Phys. Appl. Phys.* **49**, 274002 (2016).
26. Huang, Y.-F. et al. Coherent brightfield microscopy provides the spatiotemporal resolution to study early stage viral infection in live cells. *ACS Nano* **11**, 2575–2585 (2017).
27. de Wit, G., Albrecht, D., Ewers, H. & Kukura, P. Revealing compartmentalized diffusion in living cells with interferometric scattering microscopy. *Biophys. J.* **114**, 2945–2950 (2018).
28. Taylor, R. W. et al. Interferometric scattering microscopy reveals microsecond nanoscopic protein motion on a live cell membrane. *Nat. Photonics* **13**, 480–487 (2019).
29. Vala, M. et al. Nanoscopic structural fluctuations of disassembling microtubules revealed by label-free super-resolution microscopy. *Small Methods* **5**, 2000985 (2021).
30. Vamivakas, A. N. et al. Strong extinction of a far-field laser beam by a single quantum dot. *Nano Lett.* **7**, 2892–2896 (2007).
31. Kukura, P., Celebrano, M., Renn, A. & Sandoghdar, V. Imaging a single quantum dot when it is dark. *Nano Lett.* **9**, 926–929 (2009).
32. Kukura, P., Celebrano, M., Renn, A. & Sandoghdar, V. Single-molecule sensitivity in optical absorption at room temperature. *J. Phys. Chem. Lett.* **1**, 3323–3327 (2010).
33. Celebrano, M., Kukura, P., Renn, A. & Sandoghdar, V. Single-molecule imaging by optical absorption. *Nat. Photonics* **5**, 95–98 (2011).
34. Piliarik, M. & Sandoghdar, V. Direct optical sensing of single unlabelled proteins and super-resolution imaging of their binding sites. *Nat. Commun.* **5**, 4495 (2014).
35. Ortega Arroyo, J. et al. Label-free, all-optical detection, imaging, and tracking of a single protein. *Nano Lett.* **14**, 2065–2070 (2014).
36. Young, G. et al. Quantitative mass imaging of single biological macromolecules. *Science* **360**, 423–427 (2018).
37. Delor, M., Weaver, H. L., Yu, Q. & Ginsberg, N. S. Imaging material functionality through three-dimensional nanoscale tracking of energy flow. *Nat. Mater.* **19**, 56–62 (2020).
38. Su, H. et al. Dark-exciton driven energy funneling into dielectric inhomogeneities in two-dimensional semiconductors. *Nano Lett.* **22**, 2843–2850 (2022).
39. Baxter, J. M. et al. Coexistence of incoherent and ultrafast coherent exciton transport in a two-dimensional superatomic semiconductor. *J. Phys. Chem. Lett.* **14**, 10249–10256 (2023).
40. Gruber, C. G., Frey, L., Guntermann, R., Medina, D. D. & Cortés, E. Early stages of covalent organic framework formation imaged in operando. *Nature* **630**, 872–877 (2024).
41. Küppers, M., Albrecht, D., Kashkanova, A. D., Lühr, J. & Sandoghdar, V. Confocal interferometric scattering microscopy reveals 3D nanoscopic structure and dynamics in live cells. *Nat. Commun.* **14**, 1962 (2023).
42. Hsiao, Y.-T., Wu, T.-Y., Wu, B.-K., Chu, S.-W. & Hsieh, C.-L. Spinning disk interferometric scattering confocal microscopy captures millisecond timescale dynamics of living cells. *Opt. Express* **30**, 45233–45245 (2022).
43. Wrigge, G., Gerhardt, I., Hwang, J., Zumofen, G. & Sandoghdar, V. Efficient coupling of photons to a single molecule and the observation of its resonance fluorescence. *Nat. Phys.* **4**, 60–66 (2008).
44. Gerhardt, I. et al. Strong extinction of a laser beam by a single molecule. *Phys. Rev. Lett.* **98**, 033601 (2007).
45. Loudon, R. *The Quantum Theory of Light* (Oxford Univ. Press, 2000).
46. Martin, C. et al. In-line holographic microscopy with model-based analysis. *Nat. Rev. Methods Primers* **2**, 83 (2022).
47. Thiele, J. C., Pfitzner, E. & Kukura, P. Single-protein optical holography. *Nat. Photonics* **18**, 388–395 (2024).
48. Ortega Arroyo, J., Cole, D. & Kukura, P. Interferometric scattering microscopy and its combination with single-molecule fluorescence imaging. *Nat. Protoc.* **11**, 617–633 (2016).

49. Gemeinhardt, A. & et al. Label-free imaging of single proteins secreted from living cells via iSCAT microscopy. *J. Vis. Exp.* https://doi.org/10.3791/58486 (2018).
50. Kukura, P. et al. High-speed nanoscopic tracking of the position and orientation of a single virus. *Nat. Methods* **6**, 923–927 (2009).
51. Yang, Y. et al. Interferometric plasmonic imaging and detection of single exosomes. *Proc. Natl Acad. Sci. USA* **115**, 10275–10280 (2018).
52. Zhang, P. et al. Plasmonic scattering imaging of single proteins and binding kinetics. *Nat. Methods* **17**, 1010–1017 (2020).
53. Mazaheri, M. et al. iSCAT microscopy and particle tracking with tailored spatial coherence. *Optica* **11**, 1030 (2024).
54. Daaboul, G. G. et al. Digital sensing and sizing of vesicular stomatitis virus pseudotypes in complex media: a model for ebola and marburg detection. *ACS Nano* **8**, 6047–6055 (2014).
55. Utterback, J. K. et al. Operando label-free optical imaging of solution-phase ion transport and electrochemistry. *ACS Energy Lett.* **8**, 1785–1792 (2023).
56. Folie, B. D. et al. Effect of anisotropic confinement on electronic structure and dynamics of band edge excitons in inorganic perovskite nanowires. *J. Phys. Chem. A* **124**, 1867–1876 (2020).
57. Guzelturk, B. et al. Nonequilibrium thermodynamics of colloidal gold nanocrystals monitored by ultrafast electron diffraction and optical scattering microscopy. *ACS Nano* **14**, 4792–4804 (2020).
58. Delor, M. et al. Carrier diffusion lengths exceeding 1 μm despite trap-limited transport in halide double perovskites. *ACS Energy Lett.* **5**, 1337–1345 (2020).
59. Utterback, J. K. et al. Nanoscale disorder generates subdiffusive heat transport in self-assembled nanocrystal films. *Nano Lett.* **21**, 3540–3547 (2021).
60. Li, J. et al. Zwitterions in 3D perovskites: organosulfide-halide perovskites. *J. Am. Chem. Soc.* **144**, 22403–22408 (2022).
61. Weaver, H. L. et al. Detecting, distinguishing, and spatiotemporally tracking photogenerated charge and heat at the nanoscale. *ACS Nano* **17**, 19011–19021 (2023).
62. Xu, D. et al. Ultrafast imaging of polariton propagation and interactions. *Nat. Commun.* **14**, 3881 (2023).
63. Cheng, S.-W. et al. Optical imaging of ultrafast phonon–polariton propagation through an excitonic sensor. *Nano Lett.* **23**, 9936–9942 (2023).
64. Tulyagankhodjaev, J. A. et al. Room-temperature wavelike exciton transport in a van der Waals superatomic semiconductor. *Science* **382**, 438–442 (2023).
65. Lyu, P.-T. et al. Decrypting material performance by wide-field femtosecond interferometric imaging of energy carrier evolution. *J. Am. Chem. Soc.* **144**, 13928–13937 (2022).
66. Schnedermann, C. et al. Ultrafast tracking of exciton and charge carrier transport in optoelectronic materials on the nanometer scale. *J. Phys. Chem. Lett.* **10**, 6727–6733 (2019).
67. Schnedermann, C. et al. Sub-10 fs time-resolved vibronic optical microscopy. *J. Phys. Chem. Lett.* **7**, 4854–4859 (2016).
68. Sung, J. et al. Long-range ballistic propagation of carriers in methylammonium lead iodide perovskite thin films. *Nat. Phys.* **16**, 171–176 (2020).
69. Dastjerdi, H. M. et al. Optimized analysis for sensitive detection and analysis of single proteins via interferometric scattering microscopy. *J. Phys. Appl. Phys.* **55**, 054002 (2022).
70. Bohren, C. F. & Huffman, D. R. *Absorption and Scattering of Light by Small Particles* 1st edn (Wiley-VCH, 1983).
71. Kalkbrenner, T., Håkanson, U. & Sandoghdar, V. Tomographic plasmon spectroscopy of a single gold nanoparticle. *Nano Lett.* **4**, 2309–2314 (2004).
72. Jacobsen, V., Klotzsch, E. & Sandoghdar, V. Interferometric detection and tracking of nanoparticles. In *Nano Biophotonics: Science and Technology. Proc. 3rd International Nanophotonics Symposium* (eds Masuhara, H., Kawata, S. & Tokunaga, F.) 143–159 (Elsevier, 2007).
73. Taylor, R. W. & Sandoghdar, V. Interferometric scattering microscopy: seeing single nanoparticles and molecules via Rayleigh scattering. *Nano Lett.* **19**, 4827–4835 (2019).
74. Špačková, B. et al. Label-free nanofluidic scattering microscopy of size and mass of single diffusing molecules and nanoparticles. *Nat. Methods* **19**, 751–758 (2022).
75. Ignatovich, F. V. & Novotny, L. Real-time and background-free detection of nanoscale particles. *Phys. Rev. Lett.* **96**, 013901 (2006).
76. Yurdakul, C. et al. High-throughput, high-resolution interferometric light microscopy of biological nanoparticles. *ACS Nano* **14**, 2002–2013 (2020).
77. Cole, D., Young, G., Weigel, A., Sebesta, A. & Kukura, P. Label-free single-molecule imaging with numerical-aperture-shaped interferometric scattering microscopy. *ACS Photonics* **4**, 211–216 (2017).
78. Liebel, M., Hugall, J. T. & van Hulst, N. F. Ultrasensitive label-free nanosensing and high-speed tracking of single proteins. *Nano Lett.* **17**, 1277–1281 (2017).
79. Avci, O., Campana, M. I., Yurdakul, C. & Ünlü, M. S. Pupil function engineering for enhanced nanoparticle visibility in wide-field interferometric microscopy. *Optica* **4**, 247–254 (2017).
80. Brokmann, X., Coolen, L., Hermier, J.-P. & Dahan, M. Emission properties of single CdSe/ZnS quantum dots close to a dielectric interface. *Chem. Phys.* **318**, 91–98 (2005).
81. Lee, K. G. et al. A planar dielectric antenna for directional single-photon emission and near-unity collection efficiency. *Nat. Photonics* **5**, 166–169 (2011).
82. Cheng, C.-Y., Liao, Y.-H. & Hsieh, C.-L. High-speed imaging and tracking of very small single nanoparticles by contrast enhanced microscopy. *Nanoscale* **11**, 568–577 (2019).
83. Li, N. et al. Photonic resonator interferometric scattering microscopy. *Nat. Commun.* **12**, 1744 (2021).
84. Gentner, C. et al. Enhanced quantitative wavefront imaging for nano-object characterization. *ACS Nano* **18**, 19247–19256 (2024).
85. Hogenboom, D. O., DiMarzio, C. A., Gaudette, T. J., Devaney, A. J. & Lindberg, S. C. Three-dimensional images generated by quadrature interferometry. *Opt. Lett.* **23**, 783–785 (1998).
86. Diezmann, L., von, Lee, M. Y., Lew, M. D. & Moerner, W. E. Correcting field-dependent aberrations with nanoscale accuracy in three-dimensional single-molecule localization microscopy. *Optica* **2**, 985–993 (2015).
87. McGorty, R., Schnitzbauer, J., Zhang, W. & Huang, B. Correction of depth-dependent aberrations in 3D single-molecule localization and super-resolution microscopy. *Opt. Lett.* **39**, 275–278 (2014).
88. Mahmoodabadi, R. G. et al. Point spread function in interferometric scattering microscopy (iSCAT). Part I: aberrations in defocusing and axial localization. *Opt. Express* **28**, 25969–25988 (2020).
89. Kasaian, K., Mazaheri, M. & Sandoghdar, V. Long-range three-dimensional tracking of nanoparticles using interferometric scattering microscopy. *ACS Nano* **18**, 30463–30472 (2024).
90. Brooks, N. J., Liu, C.-C., Chen, Y.-H. & Hsieh, C.-L. Point spread function engineering for spiral phase interferometric scattering microscopy enables robust 3D single-particle tracking and characterization. *ACS Photonics* **11**, 5239–5250 (2024).
91. Hitzelhammer, F. et al. Unified simulation platform for interference microscopy. *ACS Photonics* **11**, 2745–2756 (2024).
92. Dastjerdi, H. M., Mahmoodabadi, R. G., Bär, M., Sandoghdar, V. & Köstler, H. PiSCAT: a Python package for interferometric scattering microscopy. *J. Open Source Softw.* **7**, 4024 (2022).
93. Wu, H.-M., Lin, Y.-H., Yen, T.-C. & Hsieh, C.-L. Nanoscopic substructures of raft-mimetic liquid-ordered membrane domains revealed by high-speed single-particle tracking. *Sci. Rep.* **6**, 20542 (2016).
94. Lin, S., He, Y., Feng, D., Piliarik, M. & Chen, X.-W. Optical fingerprint of flat substrate surface and marker-free lateral displacement detection with angstrom-level precision. *Phys. Rev. Lett.* **129**, 213201 (2022).
95. Holanová, K., Vala, M. & Piliarik, M. Optical imaging and localization of prospective scattering labels smaller than a single protein. *Opt. Laser Technol.* **109**, 323–327 (2019).
96. Jacobsen, V., Stoller, P., Brunner, C., Vogel, V. & Sandoghdar, V. Interferometric optical detection and tracking of very small gold nanoparticles at a water-glass interface. *Opt. Express* **14**, 405–414 (2006).
97. Li, Q. -Y., Lyu, P. -T., Kang, B., Chen, H. -Y. & Xu, J. -J. Label-free optical imaging of ion channel activity on living cells. Preprint at https://arxiv.org/abs/2312.16461 (2023).
98. Namink, K., Meng, X., Koper, M. T. M. & Kukura, P. & Faez, S. Electric-double-layer-modulation microscopy. *Phys. Rev. Appl.* **13**, 044065 (2020).
99. Spindler, S., Sibold, J., Gholami Mahmoodabadi, R., Steinem, C. & Sandoghdar, V. High-speed microscopy of diffusion in pore-spanning lipid membranes. *Nano Lett.* **18**, 5262–5271 (2018).
100. Robert, H. M. L. et al. Fast photothermal spatial light modulation for quantitative phase imaging at the nanoscale. *Nat. Commun.* **12**, 2921 (2021).
101. Foley, E. D. B., Kushwah, M. S., Young, G. & Kukura, P. Mass photometry enables label-free tracking and mass measurement of single proteins on lipid bilayers. *Nat. Methods* **18**, 1247–1252 (2021).
102. Witkowska, A., Spindler, S., Mahmoodabadi, R. G., Sandoghdar, V. & Jahn, R. Differential diffusional properties in loose and tight docking prior to membrane fusion. *Biophys. J.* **119**, 2431–2439 (2020).
103. Dahmardeh, M., Mirzaalian Dastjerdi, H., Mazal, H., Köstler, H. & Sandoghdar, V. Self-supervised machine learning pushes the sensitivity limit in label-free detection of single proteins below 10 kDa. *Nat. Methods* **20**, 442–447 (2023).
104. Simon, F., Weiss, L. E. & van Teeffelen, S. A guide to single-particle tracking. *Nat. Rev. Methods Primers* **4**, 66 (2024).
105. Kashkanova, A. D. et al. Precision single-particle localization using radial variance transform. *Opt. Express* **29**, 11070–11083 (2021).
106. Krishnan, M., Mojarad, N., Kukura, P. & Sandoghdar, V. Geometry-induced electrostatic trapping of nanometric objects in a fluid. *Nature* **467**, 692–695 (2010).
107. Taylor, R. W. et al. High-precision protein-tracking with interferometric scattering microscopy. *Front. Cell Dev. Biol.* **8**, 590158 (2020).
108. Shechtman, Y. Recent advances in point spread function engineering and related computational microscopy approaches: from one viewpoint. *Biophys. Rev.* **12**, 1303–1309 (2020).
109. de Wit, X. M. et al. Precise characterization of nanometer-scale systems using interferometric scattering microscopy and Bayesian analysis. *Appl. Opt.* **62**, 7205–7215 (2023).
110. Dong, J., Maestre, D., Conrad-Billroth, C. & Juffmann, T. Fundamental bounds on the precision of iSCAT, COBRI and dark-field microscopy for 3D localization and mass photometry. *J. Phys. Appl. Phys.* **54**, 394002 (2021).
111. Lin, Y.-H., Chang, W.-L. & Hsieh, C.-L. Shot-noise limited localization of single 20 nm gold particles with nanometer spatial precision within microseconds. *Opt. Express* **22**, 9159–9170 (2014).
112. Isojima, H., Iino, R., Niitani, Y., Noji, H. & Tomishige, M. Direct observation of intermediate states during the stepping motion of kinesin-1. *Nat. Chem. Biol.* **12**, 290–297 (2016).

113. Kashkanova, A. D., Blessing, M., Gemeinhardt, A., Soulat, D. & Sandoghdar, V. Precision size and refractive index analysis of weakly scattering nanoparticles in polydispersions. *Nat. Methods* **19**, 586–593 (2022).
114. Ortiz-Orruño, U., Quidant, R., van Hulst, N. F., Liebel, M. & Ortega Arroyo, J. Simultaneous sizing and refractive index analysis of heterogeneous nanoparticle suspensions. *ACS Nano* **17**, 221–229 (2023).
115. Lee, I.-B. et al. Interferometric scattering microscopy with polarization-selective dual detection scheme: capturing the orientational information of anisotropic nanometric objects. *ACS Photonics* **5**, 797–804 (2018).
116. Stoller, P., Jacobsen, V. & Sandoghdar, V. Measurement of the complex dielectric constant of a single gold nanoparticle. *Opt. Lett.* **31**, 2474–2476 (2006).
117. Daaboul, G. G. et al. High-throughput detection and sizing of individual low-index nanoparticles and viruses for pathogen identification. *Nano Lett.* **10**, 4727–4731 (2010).
118. McDonald, M. P. et al. Visualizing single-cell secretion dynamics with single-protein sensitivity. *Nano Lett.* **18**, 513–519 (2018).
119. Malay, A. D. et al. An ultra-stable gold-coordinated protein cage displaying reversible assembly. *Nature* **569**, 438–442 (2019).
120. Soltermann, F. et al. Quantifying protein–protein interactions by molecular counting with mass photometry. *Angew. Chem. Int. Ed.* **59**, 10774–10779 (2020).
121. Sendker, F. L. et al. Emergence of fractal geometries in the evolution of a metabolic enzyme. *Nature* **628**, 894–900 (2024).
122. Olerinyova, A. et al. Mass photometry of membrane proteins. *Chem* **7**, 224–236 (2021).
123. Heermann, T., Steiert, F., Ramm, B., Hundt, N. & Schwille, P. Mass-sensitive particle tracking to elucidate the membrane-associated MinDE reaction cycle. *Nat. Methods* **18**, 1239–1246 (2021).
124. Lee, S.-H. et al. Characterizing and tracking single colloidal particles with video holographic microscopy. *Opt. Express* **15**, 18275–18282 (2007).
125. Kashkanova, A. D. et al. Label-free discrimination of extracellular vesicles from large lipoproteins. *J. Extracell. Vesicles* **12**, 12348 (2023).
126. Andrecka, J., Spillane, K. M., Ortega-Arroyo, J. & Kukura, P. Direct observation and control of supported lipid bilayer formation with interferometric scattering microscopy. *ACS Nano* **7**, 10662–10670 (2013).
127. de Wit, G., Danial, J. S. H., Kukura, P. & Wallace, M. I. Dynamic label-free imaging of lipid nanodomains. *Proc. Natl Acad. Sci. USA* **112**, 12299–12303 (2015).
128. Goldfain, A. M., Garmann, R. F., Jin, Y., Lahini, Y. & Manoharan, V. N. Dynamic measurements of the position, orientation, and dna content of individual unlabeled bacteriophages. *J. Phys. Chem. B* **120**, 6130–6138 (2016).
129. Garmann, R. F., Goldfain, A. M. & Manoharan, V. N. Measurements of the self-assembly kinetics of individual viral capsids around their RNA genome. *Proc. Natl Acad. Sci. USA* https://doi.org/10.1073/pnas.1909223116 (2019).
130. Bujak, Ł. et al. Fast leaps between millisecond confinements govern ase1 diffusion along microtubules. *Small Methods* **5**, 2100370 (2021).
131. Mickolajczyk, K. J., Geyer, E. A., Kim, T., Rice, L. M. & Hancock, W. O. Direct observation of individual tubulin dimers binding to growing microtubules. *Proc. Natl Acad. Sci. USA* **116**, 7314–7322 (2019).
132. Nguyen, T. L. et al. Quantitative phase imaging: recent advances and expanding potential in biomedicine. *ACS Nano* **16**, 11516–11544 (2022).
133. Park, J.-S., Lee, I.-B., Moon, H.-M., Hong, S.-C. & Cho, M. Long-term cargo tracking reveals intricate trafficking through active cytoskeletal networks in the crowded cellular environment. *Nat. Commun.* **14**, 7160 (2023).
134. Park, J.-S. et al. Fluorescence-combined interferometric scattering imaging reveals nanoscale dynamic events of single nascent adhesions in living cells. *J. Phys. Chem. Lett.* **11**, 10233–10241 (2020).
135. Cheng, C.-Y. & Hsieh, C.-L. Background estimation and correction for high-precision localization microscopy. *ACS Photonics* **4**, 1730–1739 (2017).
136. Hsiao, Y.-T., Tsai, C.-N., Chen, T.-H. & Hsieh, C.-L. Label-free dynamic imaging of chromatin in live cell nuclei by high-speed scattering-based interference microscopy. *ACS Nano* **16**, 2774–2788 (2022).
137. Limozin, L. & Sengupta, K. Quantitative reflection interference contrast microscopy (RICM) in soft matter and cell adhesion. *ChemPhysChem* **10**, 2752–2768 (2009).
138. Sülzle, J. et al. Label-free imaging of DNA interactions with 2D materials. *ACS Photonics* **11**, 737–744 (2024).
139. Ginsberg, N. S. & Tisdale, W. A. Spatially resolved photogenerated exciton and charge transport in emerging semiconductors. *Annu. Rev. Phys. Chem.* **71**, 1–30 (2020).
140. Kennedy, C. L., Hill, A. H., Massaro, E. S. & Grumstrup, E. M. Ultrafast excited-state transport and decay dynamics in cesium lead mixed halide perovskites. *ACS Energy Lett.* **2**, 1501–1506 (2017).
141. Zhu, T., Snaider, J. M., Yuan, L. & Huang, L. Ultrafast dynamic microscopy of carrier and exciton transport. *Annu. Rev. Phys. Chem.* **70**, 219–244 (2019).
142. Akselrod, G. M. et al. Subdiffusive exciton transport in quantum dot solids. *Nano Lett.* **14**, 3556–3562 (2014).
143. Penwell, S. B., Ginsberg, L. D. S., Noriega, R. & Ginsberg, N. S. Resolving ultrafast exciton migration in organic solids at the nanoscale. *Nat. Mater.* **16**, 1136–1141 (2017).
144. Kulig, M. et al. Exciton diffusion and halo effects in monolayer semiconductors. *Phys. Rev. Lett.* **120**, 207401 (2018).
145. Balasubrahmaniyam, M. et al. From enhanced diffusion to ultrafast ballistic motion of hybrid light–matter excitations. *Nat. Mater.* **22**, 338–344 (2023).
146. Li, Y. et al. Light-assisted diazonium functionalization of graphene and spatial heterogeneities in reactivity. *J. Phys. Chem. Lett.* **10**, 4788–4793 (2019).
147. Li, W., Li, Y. & Xu, K. Azidated graphene: direct azidation from monolayers, click chemistry, and bulk production from graphite. *Nano Lett.* **20**, 534–539 (2020).
148. Li, W., Li, Y. & Xu, K. Facile, electrochemical chlorination of graphene from an aqueous NaCl solution. *Nano Lett.* **21**, 1150–1155 (2021).
149. Merryweather, A. J., Schnedermann, C., Jacquet, Q., Grey, C. P. & Rao, A. Operando optical tracking of single-particle ion dynamics in batteries. *Nature* **594**, 522–528 (2021).
150. Xu, C. et al. Operando visualization of kinetically induced lithium heterogeneities in single-particle layered Ni-rich cathodes. *Joule* **6**, 2535–2546 (2022).
151. Merryweather, A. J. et al. Operando monitoring of single-particle kinetic state-of-charge heterogeneities and cracking in high-rate Li-ion anodes. *Nat. Mater.* **21**, 1306–1313 (2022).
152. Shan, X., Patel, U., Wang, S., Iglesias, R. & Tao, N. Imaging local electrochemical current via surface plasmon resonance. *Science* **327**, 1363–1366 (2010).
153. Godeffroy, L., Ciocci, P., Lemineur, J.-F. & Kanoufi, F. Watching operando nanoscale electrochemical deposition by optical microscopy. *Curr. Opin. Electrochem.* **36**, 101165 (2022).
154. Ciocci, P., Lemineur, J.-F., Noël, J.-M., Combellas, C. & Kanoufi, F. Differentiating electrochemically active regions of indium tin oxide electrodes for hydrogen evolution and reductive decomposition reactions. An situ optical microscopy approach. *Electrochim. Acta* **386**, 138498 (2021).
155. Lemineur, J.-F., Noël, J.-M., Combellas, C. & Kanoufi, F. Optical monitoring of the electrochemical nucleation and growth of silver nanoparticles on electrode: from single to ensemble nanoparticles inspection. *J. Electroanal. Chem.* **872**, 114043 (2020).
156. Lemineur, J.-F. et al. Imaging and quantifying the formation of single nanobubbles at single platinum nanoparticles during the hydrogen evolution reaction. *ACS Nano* **15**, 2643–2653 (2021).
157. Vala, M., Palounek, D., Robert, H. M. L. & Piliarik, M. Quantitative detection of optical anisotropy of single microtubules by polarization-sensitive interferometric scattering microscopy. *J. Phys. Appl. Phys.* **54**, 204001 (2021).
158. Jiao, N., Lin, S., Feng, D., He, Y. & Chen, X.-W. Defocus-integration interferometric scattering microscopy for speckle suppression and enhancing nanoparticle detection on a substrate. *Opt. Lett.* **49**, 2841–2844 (2024).
159. Pang, G., Shen, C., Cao, L. & Hengel, A. V. D. Deep learning for anomaly detection: a review. *ACM Comput. Surv.* **54**, 1–38 (2021).
160. Jeppesen, D. K., Zhang, Q., Franklin, J. L. & Coffey, R. J. Extracellular vesicles and nanoparticles: emerging complexities. *Trends Cell Biol.* **33**, 667–681 (2023).
161. Morales-Inostroza, L. et al. An optofluidic antenna for enhancing the sensitivity of single-emitter measurements. *Nat. Commun.* **15**, 2545 (2024).
162. Wen, C., Bertosin, E., Shi, X., Dekker, C. & Schmid, S. Orientation-locked DNA origami for stable trapping of small proteins in the nanopore electro-osmotic trap. *Nano Lett.* **23**, 788–794 (2023).
163. Svirelis, J. et al. Stable trapping of multiple proteins at physiological conditions using nanoscale chambers with macromolecular gates. *Nat. Commun.* **14**, 5131 (2023).
164. Wieszczycka, K. et al. Surface functionalization — the way for advanced applications of smart materials. *Coord. Chem. Rev.* **436**, 213846 (2021).
165. Goswami, N. et al. Label-free SARS-CoV-2 detection and classification using phase imaging with computational specificity. *Light. Sci. Appl.* **10**, 176 (2021).
166. Sharonov, A. & Hochstrasser, R. M. Wide-field subdiffraction imaging by accumulated binding of diffusing probes. *Proc. Natl Acad. Sci. USA* **103**, 18911–18916 (2006).
167. Gu, M. *Advanced Optical Imaging Theory*. Springer Series in Optical Sciences Vol. 75 (Springer, 2000).
168. Xia, Q. et al. Single virus fingerprinting by widefield interferometric defocus-enhanced mid-infrared photothermal microscopy. *Nat. Commun.* **14**, 6655 (2023).
169. Yurdakul, C., Zong, H., Bai, Y., Cheng, J.-X. & Ünlü, M. S. Bond-selective interferometric scattering microscopy. *J. Phys. Appl. Phys.* **54**, 364002 (2021).
170. LIGO Scientific Collaboration and Virgo Collaborationet al. Observation of gravitational waves from a binary black hole merger. *Phys. Rev. Lett.* **116**, 061102 (2016).
171. Zumofen, G., Mojarad, N. M., Sandoghdar, V. & Agio, M. Perfect reflection of light by an oscillating dipole. *Phys. Rev. Lett.* **101**, 180404 (2008).

Acknowledgements

The authors thank their former and current team members who have contributed to the development of iSCAT over the past 20 years. The authors also thank R. Taylor and M. Miller for their comments on the manuscript. M.P. acknowledges funding by the Czech Science Foundation (project no. 23-07703S) and Operational Programme Johannes Amos Comenius financed by European Structural and Investment Funds and the Czech Ministry of Education, Youth and Sports (project no. SENDISO — CZ.02.01.01/00/22_008/0004596). N.S.G. acknowledges the support of the STROBE Center for Realtime Imaging, a National Science Foundation Science and Technology Center (grant DMR 1548924), the Center for Computational Study of Excited State Phenomena in Energy Materials (grant no. C2SEPEM) under the US Department of Energy, Office of Science, Basic Energy Sciences, Materials Sciences and Engineering Division (contract no. DE-AC02-05CH11231), as part of the Computational Materials Sciences Program, and a David and Lucile Packard Fellowship. P.K. is funded by the European Research Council Consolidator (grant PHOTOMASS 819593) and the Engineering and Physical Research Council Leadership Fellowship EP/T03419X/1. V.S. thanks the Max Planck Society for continuous financial support.

Author contributions

Introduction (V.S., N.S.G. and P.K.); Experimentation (V.S., N.S.G., P.K. and C.-L.H.); Results (V.S., N.S.G., C.-L.H., P.K. and M.P.); Applications (V.S., N.S.G., C.-L.H., P.K. and M.P.); Reproducibility and data deposition (M.P., V.S. and C.-L.H.); Limitations and optimizations (V.S.); Outlook (V.S. and N.S.G.); overview of the Primer (V.S.).

Competing interests

P.K. is founder, shareholder and non-executive director of Refeyn Ltd. V.S. is a member of the Scientific Advisory Board of Bruker Switzerland AG. N.S.G., C.-L.H. and M.P. declare no competing interests.

Additional information

Peer review information *Nature Reviews Methods Primers* thanks the anonymous reviewers for their contribution to the peer review of this work.